Article

Neuron

Congenital Nystagmus Gene FRMD7 Is Necessary for Establishing a Neuronal Circuit Asymmetry for Direction Selectivity

Highlights

- FRMD7 is required for the horizontal optokinetic reflex in mice as in humans
- Horizontal direction selectivity is lost in the retina of *FRMD7* mutant mice
- Asymmetry of inhibitory inputs to horizontal DS cells is lost in *FRMD7* mutant mice
- FRMD7 is expressed in *ChAT*-expressing cells in the retina of mice and primates

Authors

Keisuke Yonehara, Michele Fiscella, Antonia Drinnenberg, ..., Francis Munier, Andreas Hierlemann, Botond Roska

Correspondence

botond.roska@fmi.ch

In Brief

Yonehara et al. show that *FRMD7*, a gene that is defective in human congenital nystagmus, is required in the mouse retina to establish spatially asymmetric inhibitory inputs from starburst cells to horizontal direction-selective ganglion cells.

Yonehara et al., 2016, Neuron *89*, 177–193
January 6, 2016
http://dx.doi.org/10.1016/j.neuron.2015.11.032

CellPress

Neuron
Article

Congenital Nystagmus Gene FRMD7 Is Necessary for Establishing a Neuronal Circuit Asymmetry for Direction Selectivity

Keisuke Yonehara,[1,9,10] Michele Fiscella,[2,10] Antonia Drinnenberg,[1,3,10] Federico Esposti,[1] Stuart Trenholm,[1] Jacek Krol,[1] Felix Franke,[2] Brigitte Gross Scherf,[1] Akos Kusnyerik,[4] Jan Müller,[2] Arnold Szabo,[5] Josephine Jüttner,[1] Francisco Cordoba,[6] Ashrithpal Police Reddy,[1] János Németh,[4] Zoltán Zsolt Nagy,[4] Francis Munier,[7] Andreas Hierlemann,[2] and Botond Roska[1,8,*]

[1]Neural Circuit Laboratories, Friedrich Miescher Institute for Biomedical Research, Maulbeerstrasse 66, 4058 Basel, Switzerland
[2]Bio Engineering Laboratory, Department of Biosystems Science and Engineering of ETH Zurich, Mattenstrasse 26, 4058 Basel, Switzerland
[3]University of Basel, Petersplatz 1, 4003 Basel, Switzerland
[4]Department of Ophthalmology, Semmelweis University, Mária u. 39, 1085 Budapest, Hungary
[5]Department of Human Morphology and Developmental Biology, Faculty of Medicine, Semmelweis University, Tűzoltó u. 58, 1094 Budapest, Hungary
[6]Laboratory and Animal Services, Novartis Institute for Biomedical Research, Fabrikstrasse 28, 4056 Basel, Switzerland
[7]Jules-Gonin Eye Hospital, Avenue de France 15, 1000 Lausanne, Switzerland
[8]Department of Ophthalmology, University of Basel, Mittlere Strasse 91, 4031 Basel, Switzerland
[9]Present address: The Danish Research Institute of Translational Neuroscience – DANDRITE, Nordic EMBL Partnership for Molecular Medicine, Department of Biomedicine, Aarhus University, Ole Worms Alle 3, 8000 Aarhus C, Denmark
[10]Co-first author
*Correspondence: botond.roska@fmi.ch
http://dx.doi.org/10.1016/j.neuron.2015.11.032

SUMMARY

Neuronal circuit asymmetries are important components of brain circuits, but the molecular pathways leading to their establishment remain unknown. Here we found that the mutation of FRMD7, a gene that is defective in human congenital nystagmus, leads to the selective loss of the horizontal optokinetic reflex in mice, as it does in humans. This is accompanied by the selective loss of horizontal direction selectivity in retinal ganglion cells and the transition from asymmetric to symmetric inhibitory input to horizontal direction-selective ganglion cells. In wild-type retinas, we found FRMD7 specifically expressed in starburst amacrine cells, the interneuron type that provides asymmetric inhibition to direction-selective retinal ganglion cells. This work identifies FRMD7 as a key regulator in establishing a neuronal circuit asymmetry, and it suggests the involvement of a specific inhibitory neuron type in the pathophysiology of a neurological disease.

INTRODUCTION

Neuronal circuit asymmetries are important building blocks of the nervous system. Sensory circuits rely on circuit asymmetries to detect external features, like the position of sound sources, the orientation of visual objects, or the direction of visual motion. In both invertebrates and vertebrates, neurons have been identified that respond selectively to the direction of visual motion as follows: vigorously to motion in a preferred direction, but only weakly to motion in the opposite null direction (Borst and Euler, 2011). Direction-selective neurons are already present at the sensory periphery, in the lobula and lobular plate of flies and in the retina of vertebrates (Borst and Helmstaedter, 2015). Retinal direction-selective neurons have preferred directions and corresponding circuit asymmetries along the cardinal directions. Due to their accessibility for physiological recordings and genetic manipulation, these circuits serve as model systems for understanding the formation of neuronal circuit asymmetries (Wei and Feller, 2011). However, the molecules establishing the asymmetry of direction-selective circuits along the cardinal axes remain unknown.

A potential source for identifying candidate molecules involved in the development of cardinal direction selectivity are monogenic diseases, which disrupt human visual behaviors that depend on the activity of direction-selective retinal cells. A visually guided behavior that relies on the activity of retinal direction-selective neurons is the optokinetic reflex (Osterhout et al., 2015; Oyster et al., 1972; Sun et al., 2015; Yoshida et al., 2001). The optokinetic reflex is initiated by a visual scene drifting on the retina, which triggers the eye to follow it, thus keeping the image stable on the retina. The optokinetic reflex works together with the vestibulo-ocular reflex, in which eye movement is initiated by head or body motion, to stabilize the gaze while the animal moves its head or entire body (Schweigart et al., 1997). These two reflexes, driven by visual and body motions, are complementary. The optokinetic reflex dominates gaze stabilization at lower speeds and the vestibular reflex does so at higher

speeds (van Alphen et al., 2001; Faulstich et al., 2004). The optokinetic reflex can be separated from the vestibulo-ocular reflex if the head is fixed in place (Bryan and Angelaki, 2009).

A neurological disease in which the optokinetic reflex is disturbed is idiopathic congenital nystagmus. Individuals with idiopathic congenital nystagmus, which occurs in 1 in 1,500 humans, have impaired eye movements resulting in impaired vision (Gottlob and Proudlock, 2014). In 70% of the detected cases, mutations in the *FRMD7* gene on the X chromosome have been reported (Tarpey et al., 2006). Individuals without a functional *FRMD7* allele have involuntary horizontal eye oscillations (nystagmus) and lack the optokinetic reflex along the horizontal axis (Thomas et al., 2008, 2011). In contrast, along the vertical axis no nystagmus can be observed and the optokinetic reflex is unaffected. The symptoms begin in early childhood at an age of 2–3 months. While *FRMD7* expression has been localized to the retina and the vestibular system (Tarpey et al., 2006; Thomas et al., 2011), the neuronal circuit dysfunction responsible for the symptoms of the disease is unknown.

In the retina of mammals, including mice, three classes of direction-selective ganglion cells (DS cells) have been described as follows: on-off DS cells, on DS cells, and off DS cells (Sanes and Masland, 2015). The on-off cells respond to both light increments and decrements, while on cells respond only to increments and off cells only to decrements. The on-off DS cells consist of four types with preferred directions corresponding to each of the four cardinal directions (inferior, superior, temporal, and nasal; note that throughout the text the direction of motion is defined based on the direction of motion on the retina). The on DS cells can be classified into three types, with preferred motion directions being inferior, superior, and temporal. The off DS cells prefer motion in the inferior direction. Most on DS cells and a type of on-off DS cell are tuned to slow motion, while most on-off DS cells and a group of on DS cell prefer faster motion (Dhande et al., 2013; Gauvain and Murphy, 2015). DS cell types in the mouse retina are genetically determined populations of neurons: they can be labeled by distinct molecular markers and they form retinal mosaics (Sanes and Masland, 2015).

It has been suggested that slow-motion-tuned DS cells are the main source of direction-selective input driving the optokinetic reflex in response to slow drifts of the visual scene (Oyster et al., 1972). Indeed, the optokinetic reflex is lost when retinal direction selectivity is abolished by genetic ablation of starburst cells, which are a key circuit component of the retinal direction-selective circuit (Yoshida et al., 2001). Slow-motion-tuned on and on-off DS cells project their axons to the nuclei of the accessory optic system (Dhande et al., 2013; Yonehara et al., 2009), which consists of the medial terminal nucleus (MTN), the lateral terminal nucleus (LTN), and the nucleus of the optic tract (NOT)/dorsal terminal nucleus (DTN) complex (Giolli et al., 2006; Simpson, 1984; Figure 6C). In mice, the MTN receives retinal inputs from superior and inferior motion-preferring on DS cells (Dhande et al., 2013; Yonehara et al., 2009), and inferior motion-preferring on-off DS cells (Kay et al., 2011); the NOT/DTN complex receives retinal inputs from temporal motion-preferring on and on-off DS cells (Dhande et al., 2013). Direction-selective responses with preferred directions along the vertical axis have been recorded in the MTN and LTN, while responses with preferred directions along the horizontal axis have been recorded in the NOT/DTN complex (Soodak and Simpson, 1988). Activity in the NOT/DTN complex has been shown to be required selectively for the horizontal optokinetic reflex (Hoffmann and Fischer, 2001), while MTN activity is required for the vertical optokinetic reflex (Sun et al., 2015). The accessory optic system is conserved across species, as the MTN and NOT/DTN have been anatomically identified in a number of species including mouse, rabbit, cat, monkey, and human (Giolli et al., 2006; Simpson, 1984).

The retinal circuitry underlying the direction-selective responses of on-off and on DS cells has been investigated in detail. DS cells receive excitatory input from glutamatergic bipolar cells, as well as inhibitory and excitatory inputs from starburst amacrine cells. Starburst cells release both GABA and acetylcholine (Vaney et al., 2012). The glutamatergic excitatory input from bipolar cells and the cholinergic excitatory input, which likely arrives via paracrine secretion from starburst cells (Briggman et al., 2011), are not direction selective (Lee et al., 2010; Yonehara et al., 2013; but see Pei et al., 2015). The GABAergic inhibitory input from starburst cells is spatially asymmetric: in response to motion in the null direction, inhibitory input is maximal; in response to motion in the preferred direction, inhibitory input is minimal (Vaney et al., 2012). Furthermore, active integration mechanisms in the dendrites of DS cells sharpen the spiking output of DS cells (Oesch et al., 2005; Sivyer and Williams, 2013; Trenholm et al., 2014). With the exception of the responses of a single on-off DS cell type to slow motion (Trenholm et al., 2011) and the responses of the off DS cell type (Kim et al., 2008), the inhibitory input from starburst cells is necessary for the direction-selective responses of DS cells (Fried et al., 2002; Yoshida et al., 2001).

The direction selectivity of the inhibitory input to DS cells relies on two features of the retinal circuit. The first feature is an asymmetric neurotransmitter release from starburst cells. Starburst cell processes radiate away from the soma; they act both as dendrites, receiving input from bipolar cells and other starburst cells, and as axons, providing input to DS cells and other starburst cells (Famiglietti, 1991; Kim et al., 2014). A starburst cell process preferentially releases GABA if motion occurs in a centrifugal direction along the process, from the soma to the tip (Euler et al., 2002). This asymmetric release could be due to inputs from different types of bipolar cells with different temporal characteristics along the starburst cell process (Kim et al., 2014), an excitability gradient (Gavrikov et al., 2003; Hausselt et al., 2007), or inhibitory interactions between starburst cells (Lee and Zhou, 2006). This asymmetry is radial, centered on each starburst soma, and likely has no information about the cardinal directions. Therefore, the disruption of its development would likely result in a decrease in direction selectivity along all four cardinal directions. The second circuit feature, on which direction selectivity relies, is the spatially asymmetric inhibitory connectivity between starburst cells and DS cell types (Briggman et al., 2011; Fried et al., 2002). The angle of a starburst cell process relative to the cardinal directions in the retina determines the connectivity between the starburst cell process and the DS cell type (Figures 1A and 1B). For instance, starburst processes that point nasally connect to DS cell types preferring temporal motion, and starburst processes that point superiorly connect to DS types preferring inferior motion (Briggman et al., 2011). This

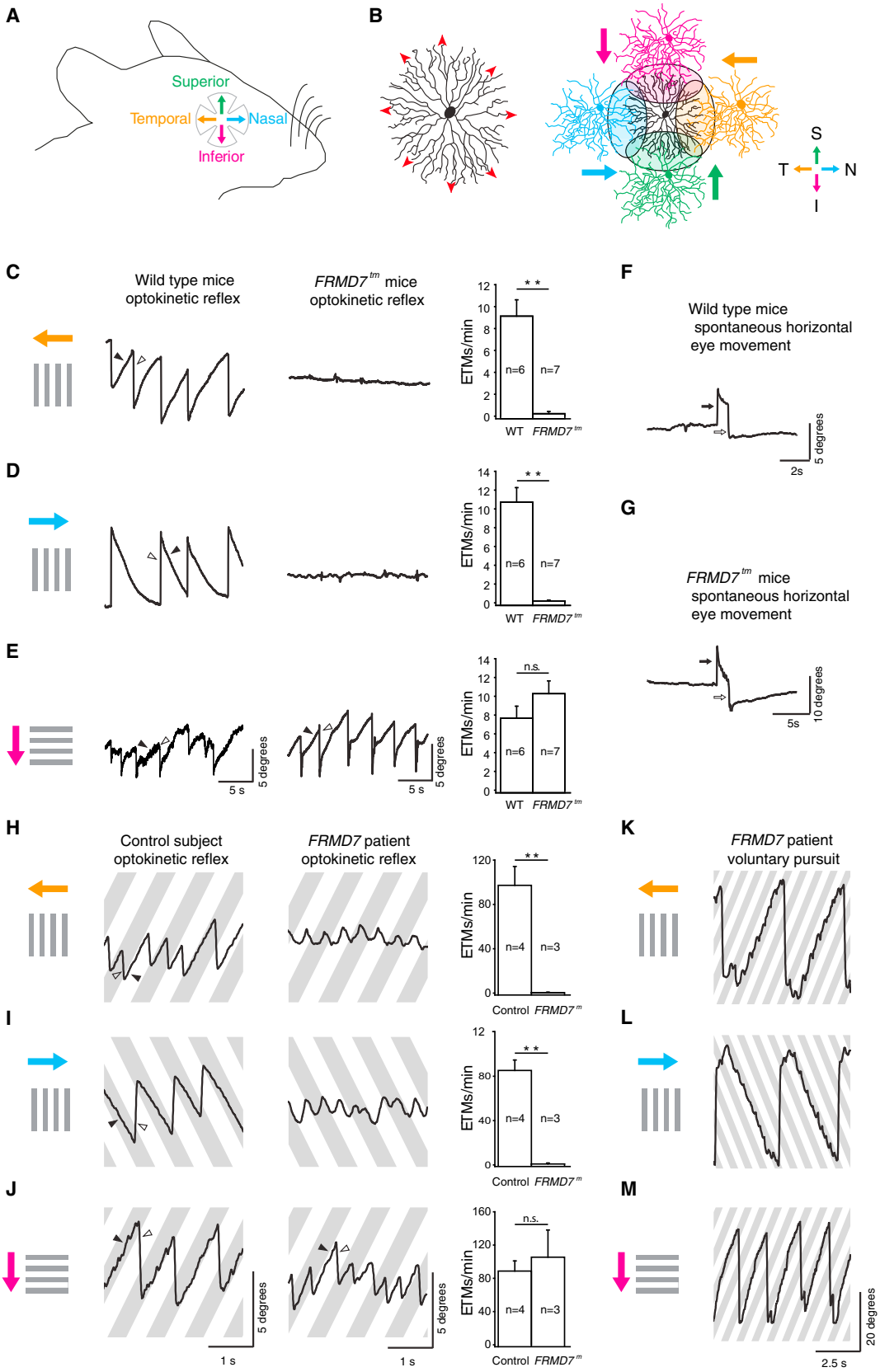

(legend on next page)

spatially asymmetric connectivity is believed to be necessary for defining cardinal direction selectivity. Developmental disruption could potentially result in the loss of direction selectivity in specific directions or combinations of directions.

Spatially asymmetric inhibitory connectivity between starburst cells and DS cells forms independent of visual activity or spontaneous retinal waves (Elstrott et al., 2008), and occurs rapidly between post-natal day 6 (P6) and eye opening, from previously established symmetric inputs (Wei et al., 2011; Yonehara et al., 2011). Molecules responsible for positioning DS cell dendrites, for establishing bipolar cell input, and for defining the morphology and spacing of starburst cells have been described already (Duan et al., 2014; Sun et al., 2013), and molecules responsible for creating centrifugal direction selectivity in starburst cell processes have been proposed (Gavrikov et al., 2003). While disruption of some of these molecules results in decreased tuning of direction-selective responses (Sun et al., 2013), no molecules have been identified that are necessary for motion detection in specific directions (Duan et al., 2014; Gavrikov et al., 2003; Sun et al., 2013). Therefore, the molecular pathway responsible for setting up the circuit asymmetry along the cardinal directions has remained unidentified.

Recently, using a transcriptional map of adult retinal cell types in mice, we found that FRMD7, the gene in which mutations result in the lack of the horizontal optokinetic reflex in humans, is enriched in starburst cells (Siegert et al., 2012), suggesting that direction-selective circuits in the retina could be involved in the disease. The *FRMD7* gene encodes a member of the FERM domain family of proteins (Moleirinho et al., 2013) and has been implicated in the reorganization of the cytoskeleton (Pu et al., 2013). Here we investigate a potential link between the function of FRMD7, the development of retinal direction selectivity, and the lack of the horizontal optokinetic reflex in FRMD7-based congenital nystagmus.

RESULTS

FRMD7 Is Required for the Horizontal Optokinetic Reflex in Mice

We compared the optokinetic reflex and spontaneous eye movements of wild-type and *FRMD7* hypomorphic mutant (*FRMD7^{tm}*; Experimental Procedures; Figure S1) mice (Figures 1 and S2). Head-fixed mice were presented with drifting gratings while their eye movements were tracked with a camera. In wild-type mice, a strong optokinetic reflex could be elicited in nasal, temporal, and inferior directions (Figures 1C–1E). The reflex was weak in the superior direction (Figure S2A), as has been reported previously (Yonehara et al., 2009). Similar to human subjects with *FRMD7* mutation (Thomas et al., 2011; Figures 1H–1J and S2), *FRMD7^{tm}* mice lacked the horizontal optokinetic reflex, both in the nasal and temporal directions (Figures 1C and 1D; Movie S1), but the vertical inferior optokinetic reflex of *FRMD7^{tm}* mice was similar to that of wild-type mice (Figure 1E). The absence of the horizontal optokinetic reflex did not appear to arise from an inability of the mice to move their eyes horizontally, as we observed spontaneous horizontal eye movements in wild-type and *FRMD7^{tm}* mice (Figures 1F and 1G). Similarly, human subjects with *FRMD7* mutation could perform voluntary horizontal eye movements (Figures 1K and 1L). We observed no spontaneous oscillatory eye movements (nystagmus) in *FRMD7^{tm}* mice. These results suggest that one of the symptoms, the lack of the horizontal optokinetic reflex, is shared between *FRMD7^{tm}* mice and human subjects with *FRMD7* mutation and that the motor circuits of both humans and mice remain capable of moving the eyes horizontally.

Lack of Horizontal Direction Selectivity in the Retina of *FRMD7^{tm}* Mice

We investigated whether the lack of the horizontal optokinetic reflex is accompanied by altered retinal activity in *FRMD7^{tm}* mice. We recorded the spiking activity of retinal ganglion cells in wild-type and *FRMD7^{tm}* mice using microelectrode arrays. The retina was stimulated with light flashes and bars moving in different directions and at different velocities. Light flashes were used to segregate on and on-off cells, motion in different directions was used to determine direction selectivity, and different velocities were used to differentiate between slow- and fast-motion-preferring DS cells (Experimental Procedures). Retinas of *FRMD7^{tm}* mice responded well to both light flashes and slow and fast motions (Figures S3A–S3C). However, in *FRMD7^{tm}* mice the fractions of cells with direction-selective responses were significantly lower (by 52% and 44%) than in wild-type

Figure 1. Horizontal Optokinetic Reflex Is Absent in *FRMD7^{tm}* Mice and in Human Subjects with FRMD7 Mutation

(A) Retinal cardinal axes are shown.

(B) (Left) A schematic of a starburst cell showing the direction of centrifugal motion (red arrowheads) that evokes transmitter release. (Right) Spatial organization of synaptic connectivity between a starburst cell (center, black) and four types of DS cells, color coded according to their preferred directions (colored arrows), is shown.

(C–E) Optokinetic reflex eye movements produced by wild-type (WT, left) and *FRMD7^{tm}* (middle) mice in response to motion in the temporal (top), nasal (middle), and inferior (bottom) directions on the retina. Gray bars represent the motion stimulus and arrows colored according to the color code in (A) indicate the motion direction on the retina. The right column shows the quantification of optokinetic reflex eye-tracking movements per minute (ETMs, Supplemental Experimental Procedures) for WT and *FRMD7^{tm}* mice in the three directions. Filled and open arrowheads indicate the slow phase and fast phase of eye movements, respectively.

(F and G) Spontaneous eye movements in WT (F) and *FRMD7^{tm}* (G) mice along horizontal axes. Open and filled arrows indicate eye movements to the left and right, respectively.

(H–J) Optokinetic reflex in a control human subject (left) and a subject with *FRMD7* mutation (middle) in response to motion in the temporal (top), nasal (middle), and inferior (bottom) directions on the retina. Gray bars represent the motion stimulus and arrows colored according to the color code in (A) indicate the motion direction on the retina. The right column shows the quantification of optokinetic reflex ETMs for control human subjects and for subjects with *FRMD7* mutation in the three directions (Supplemental Experimental Procedures). Filled and open arrowheads indicate slow phase and fast phase of eye movements, respectively.

(K–M) Voluntary pursuit movements in a human subject with *FRMD7* mutation in response to the motion protocols as in (H)–(J). Data are shown as mean ± SEM; n refers to the number of animals in (C)–(E) and subjects in (H)–(J).

See also Figures S1 and S2 and Movie S1.

mice when stimulated with fast and slow motions, respectively (Figure S3C).

In wild-type retinas, we recorded direction-selective responses along both the horizontal and the vertical axes: we identified fast-motion-tuned DS cells, preferring motion along the cardinal directions, and slow-motion-tuned DS cells types, preferring superior, inferior, or temporal motion (Figure 2). Similarly we found on-off DS cells preferring motion along the cardinal directions and on DS cells preferring mainly superior, inferior, or temporal motion (Figures S4A–S4C). Strikingly, in *FRMD7^{tm}* mice, the fraction of (temporal or nasal) horizontal motion-preferring DS cells decreased by 95% (fast motion) and 93% (slow motion) compared to wild-type mice (Figure 2). The nearly complete lack of direction selectivity along the horizontal axis was found in both on and on-off DS cells (Figures S4A–S4C). Nevertheless, in *FRMD7^{tm}* mice, the number of vertical motion-preferring direction-selective cells relative to all recorded ganglion cells remained similar to wild-type (Figure 2F). Thus, the loss of *FRMD7* leads to the specific loss of horizontal direction-selective responses in the retina.

FRMD7 Is Selectively Expressed in Starburst Cells in the Retina

A transcriptional map of adult retinal cell types in mice suggested that FRMD7 is enriched in adult starburst cells (Siegert et al., 2012). To test whether starburst cells specifically express *FRMD7*, we performed double-label quantitative fluorescence in situ hybridization with antisense probes for *FRMD7* mRNA and *ChAT* mRNA at different developmental times (Figures 3A, 3B, and S5A). *ChAT* is a specific marker for starburst cells. Both *FRMD7* and *ChAT* expressions were first observed at P3. Once expressed, *FRMD7* and *ChAT* mRNAs were co-localized in the same cells, both in the ganglion cell layer and in the inner nuclear layer. We did not detect signals with control sense probe for *FRMD7* mRNA (Figures 3C and S5B).

We obtained further evidence that *FRMD7* expression is specific to starburst cells using immunohistochemistry: in *FRMD7^{tm}* mice, *lacZ* is inserted into the locus between exons 3 and 4. By performing antibody staining against LacZ and ChAT, we confirmed that the expression of LacZ is restricted to ChAT-positive cells in the retina (Figure S1F). Thus, in the developing and adult retina, *FRMD7* is specifically expressed in starburst cells, the key cell type for establishing retinal direction selectivity.

Starburst Cells in *FRMD7^{tm}* Mice Have Normal Morphology and Stratification

We then tested whether the morphology of starburst cells is affected in *FRMD7^{tm}* mice. Starburst cell processes stratify into on and off sublayers as early as P3, and bistratified ganglion cell dendrites follow these processes as early as P3–P4 (Stacy and Wong, 2003). The on-off DS cells receive inhibitory input from starburst cells already at P4 (Wei et al., 2011). The density of starburst cell somas, labeled with an antibody against ChAT, was similar in wild-type and *FRMD7^{tm}* mice, both in the ganglion cell and in the inner plexiform layer (Figures 3D and 3E). Furthermore, starburst cells extended their processes to the same depths in the inner plexiform layer in wild-type and *FRMD7^{tm}* mice (Figure 3F).

To examine the morphology of individual starburst cells, we sparsely labeled them in both control and *FRMD7^{tm}* mice. For this we used control *Chat-Cre* mice and *FRMD7^{tm};Chat-Cre* mice and infected the retina in vivo with conditional adeno-associated virus (AAV), expressing a mutant TVA receptor (TVA66T) (Miyamichi et al., 2013), and EnvA-coated SADΔG-GFP rabies virus. Confocal imaging of infected starburst cells revealed that the gross morphology of starburst cells, the size of the dendritic field, the symmetry of the processes, and the number of primary processes were similar in control and *FRMD7^{tm}* mice (Figures 3G and 3H).

To visualize the output synapses of starburst cells, we labeled starburst cells with a fluorescently tagged presynaptic marker in both control and *FRMD7^{tm}* mice. We infected the retinas of control *Chat-Cre* mice and *FRMD7^{tm};Chat-Cre* mice in vivo with AAV, expressing GFP-tagged synaptophysin in the presence of Cre recombinase. Confocal imaging of the infected starburst cells indicated no sign of abnormal density of output synapses in *FRMD7^{tm}* mice (Figure 3I).

Loss of the Asymmetry of Inhibitory Inputs to Horizontal DS Cells

There could be several reasons for the lack of horizontal direction selectivity in the *FRMD7^{tm}* retinas. First, it is possible that horizontal DS cells are lost in *FRMD7^{tm}* mice. Alternatively, horizontal DS cells might remain present, but lose their horizontal direction-selective responses due to changes in the retinal circuit. To further examine the circuit mechanism underlying the lack of horizontal direction selectivity, we used *Hoxd10-GFP* mice, in which the three on DS cell types and one temporal on-off DS cell type, but no other retinal cell type, are genetically labeled (Dhande et al., 2013). All GFP-labeled ganglion cells in *Hoxd10-GFP* mice project to the nuclei of the accessory optic system and prefer slow motion. We crossed *FRMD7^{tm}* mice with *Hoxd10-GFP* mice and compared the labeled ganglion cell population with that of control *Hoxd10-GFP* mice. We found that the density of GFP-labeled cells was unchanged in *FRMD7^{tm};Hoxd10-GFP* mice compared to control mice (Figures S6B and S6C), suggesting that cells with the genetic identity of wild-type horizontal DS cells are not lost in the *FRMD7^{tm}* background.

The lack of horizontal direction selectivity in *FRMD7^{tm}* retinas can be a sign either of no motion responses or of responses that have similar magnitudes in all motion directions in ganglion cells that have the genetic identity of wild-type horizontal DS cells. The third possibility, that horizontal motion-preferring DS cells are converted to vertical motion-preferring cells in *FRMD7^{tm}* retinas, is not likely since the number of vertical DS cells does not increase in *FRMD7^{tm}* retinas compared to wild-type (Figure 2F). We performed two-photon targeted patch-clamp recordings from GFP-labeled cells (Figure S6A) in isolated retinas of control *Hoxd10-GFP* mice and *FRMD7^{tm};Hoxd10-GFP* mice. We recorded spiking activity, as well as inhibitory and excitatory currents, while stimulating the retina with light spots, either flashed to the receptive field center or moving across the retina in eight different directions (Figure 4).

We first analyzed GFP-labeled on-off cells since these cells belong to a single horizontal motion-preferring DS cell type in

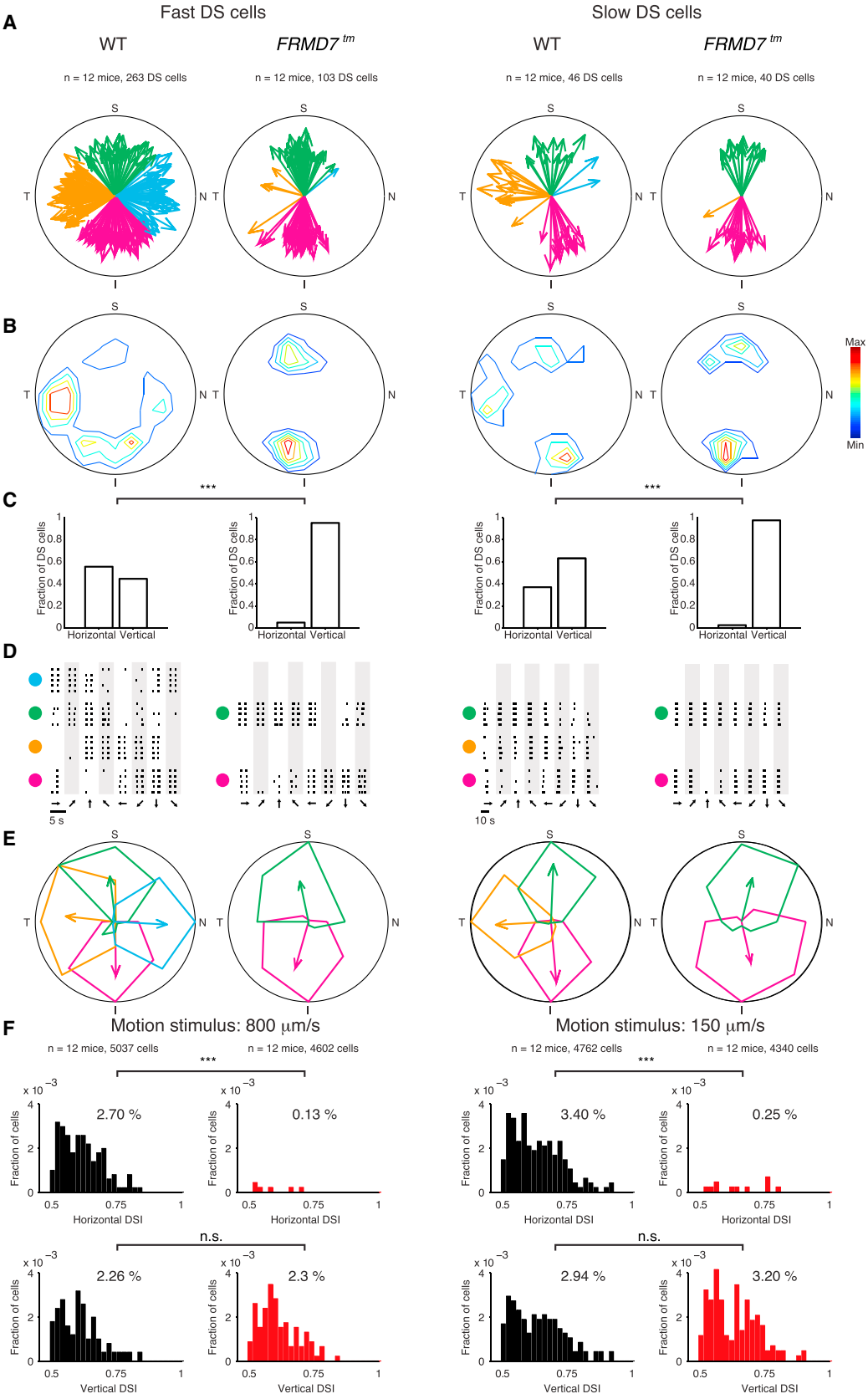

(legend on next page)

control *Hoxd10-GFP* retinas. Targeting GFP-labeled on-off cells in *FRMD7^{tm}*;*Hoxd10-GFP* retinas, therefore, allows for identifying ganglion cells with the genetic identity of wild-type horizontal DS cells in the *FRMD7^{tm}* background. In control mice, spike recordings performed in cell-attached mode confirmed that GFP-labeled on-off cells respond to motion stimulation and preferred temporal motion (Figures 4A and 4E). In contrast, in *FRMD7^{tm}*;*Hoxd10-GFP* mice, GFP-labeled on-off cells lacked direction selectivity by not responding to motion stimulation in any direction (Figures 4B and 4E). However, the spike responses to flashed spots remained similar to those in control mice (Figure 4E). To understand the cause for the lack of direction selectivity, we recorded excitatory and inhibitory currents from GFP-labeled on-off cells in whole-cell patch-clamp mode after the spike recording from the same cells was finished. The excitatory inputs during motion stimulation remained similar to those in the control (Figure S6E). As far as inhibition, in control retinas, GFP-labeled on-off cells received asymmetric inhibitory inputs: the inhibition was largest when the stimulus moved nasally, the null direction. In contrast, in *FRMD7^{tm}*;*Hoxd10-GFP* mice, GFP-labeled non-DS on-off cells received symmetric inhibitory inputs: the magnitude of inhibition was similar across all directions and its value ranged between the nasal and temporal values of the motion-evoked inhibition measured in control retinas (Figures 4A, 4B, 4E, and S6I). These results suggest that the increased inhibition evoked by motion in the temporal direction abolishes motion-evoked spiking activity in GFP-labeled on-off cells and, furthermore, that the decreased magnitude of inhibition in the nasal direction is enough to suppress spiking in this direction.

We then analyzed the spiking activity of GFP-labeled on cells that were not vertically tuned. While these cells preferred horizontal motion in control mice (Figures 4C and 4F), they responded in all motion directions, indiscriminately, in *FRMD7^{tm}*;*Hoxd10-GFP* mice (Figures 4D and 4F). Analysis of the inhibitory input to these cells revealed that the asymmetry of the inhibition was significantly reduced along the horizontal axis (Figure 4F). The magnitude of the inhibition lay between the nasal and temporal values of the motion-evoked inhibition measured in control retinas, but closer to the temporal side (Figure S6I). The distribution of the motion-evoked inhibitory responses of on cells was significantly different from that of on-off cells in *FRMD7^{tm}*;*Hoxd10-GFP* retinas (Figure S6J). Comparing the timing of spiking, inhibition, and excitation evoked by motion stimulation in on-off and on cells revealed that, while inhibition and excitation temporally overlapped in the non-spiking on-off cells, the spiking in on cells corresponded to the sustained phase of excitation, suggesting that the reduced inhibition is unable to block the effect of this part of the excitatory input (Figures S6F–S6H). Taken together, in both GFP-labeled on-off and on cells (which were not tuned vertically) of *FRMD7^{tm}*;*Hoxd10-GFP* mice, the inhibitory input is symmetric. Depending on the magnitude and time course of excitation and inhibition, the symmetric inhibition either blocks spiking in all motion directions, as in on-off cells, or leads to indiscriminate spiking in all motion directions, as found in on cells.

To examine whether the dendrites of GFP-labeled non-DS on-off and on cells in *FRMD7^{tm}*;*Hoxd10-GFP* mice were mistargeted, we filled the cells with neurobiotin during the recording and subsequently reconstructed their dendritic stratification. Similar to GFP-labeled cells in control *Hoxd10-GFP* mice, the dendrites of the recorded GFP-labeled non-DS on-off and on cells in retinas of *FRMD7^{tm}*;*Hoxd10-GFP* mice co-stratified with either the proximal or both the proximal and distal ChAT-positive strata (Figures 4G–4J). This is consistent with a view that the symmetric inhibitory input to GFP-labeled non-DS cells is delivered by starburst cells in *FRMD7^{tm}* mice.

We encountered only a few GFP-labeled vertical motion-preferring DS cells in *Hoxd10-GFP* retinas, both in the control and *FRMD7^{tm}* background. Therefore, we used a different approach to label vertical DS cells and compare their tuning in wild-type and *FRMD7^{tm}* retinas. We injected a retrograde fluorescent tracer, cholera toxin subunit B Alexa 488 conjugate, into the MTN of wild-type and *FRMD7^{tm}* mice. We performed two-photon targeted patch-clamp recordings from Alexa 488-labeled cells in isolated retinas (Figures 5 and S6D). We recorded spiking activity in cell-attached mode and inhibitory currents in whole-cell mode. The MTN back-labeled ganglion cells in *FRMD7^{tm}* retinas had direction-selective spiking responses and inhibitory currents similar to the MTN back-labeled ganglion cells recorded in wild-type retinas. The preferred direction of the spiking responses and inhibitory currents opposed each other and pointed either superior or inferior (Figure 5). Thus, in *FRMD7^{tm}* mice, vertical motion-preferring on DS cells are direction selective similar to wild-type mice.

Figure 2. Lack of Horizontal Direction Selectivity in the Retina of *FRMD7^{tm}* Mice

The figure shows data obtained with microelectrode arrays. In (A)–(E), the left two columns correspond to cells tuned to fast motion and the right two columns to cells tuned to slow motion (Supplemental Experimental Procedures). The radius of each circle corresponds to direction selectivity index (DSI) = 1.

(A) Polar plots showing the preferred directions (direction of arrow) and DSI (length of an arrow) of individual DS cells (DSI > 0.5, each recorded DS cell is represented by an arrow) in WT and *FRMD7^{tm}* retinas. The color code shows the different directions according to Figure 1A.

(B) Contour plots showing the density of DS cells at different DSIs and preferred directions. Red indicates maximal density.

(C) The proportions of horizontal (nasal and temporal) and vertical (superior and inferior) motion-preferring DS cells in WT and *FRMD7^{tm}* retinas are shown.

(D) Raster plots showing the spike responses (each black line is a spike) of example DS cells in WT and *FRMD7^{tm}* retinas in response to motion in eight different directions, indicated by the arrows at the bottom of the plot. Responses to stimulus repetitions (n = 5) are shown in different rows. Large colored dots indicate the preferred directions of DS cells according to the color code in Figure 1A.

(E) Polar plots of the normalized mean spike numbers of cells shown in (D). The preferred direction and DSI of each cell are shown by the direction and length of the corresponding (color-coded) arrow.

(F) Distributions of the horizontal (top) and vertical (bottom) DSIs (Supplemental Experimental Procedures) of DS cells in WT (black) and *FRMD7^{tm}* (red) retinas for fast (left) and slow (right) stimulus speeds are shown.

See also Figures S3 and S4.

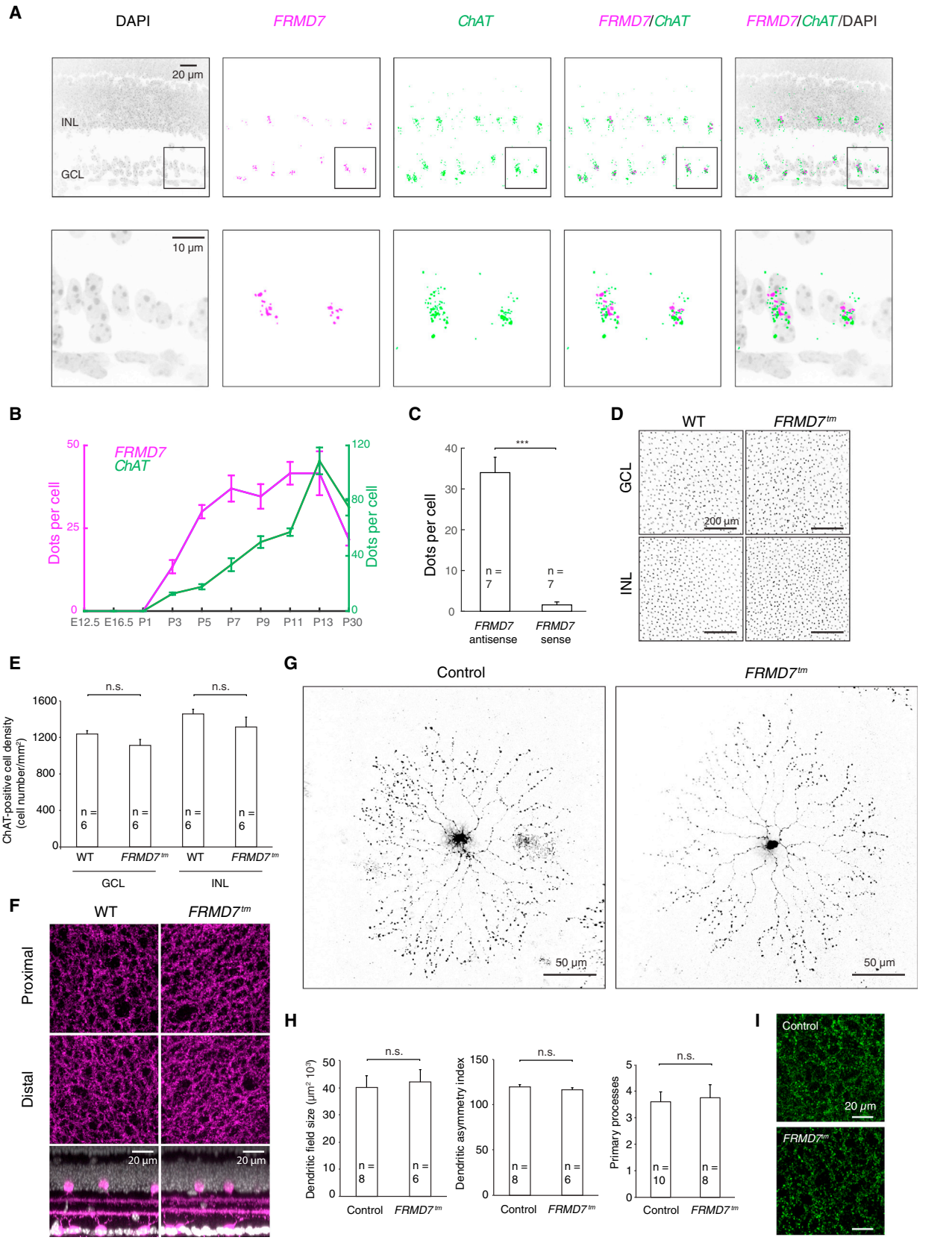

(legend on next page)

Developmental Time Window in which FRMD7 Is Required for Establishing Horizontal Direction Selectivity

We investigated whether FRMD7 is required for the formation or for the maintenance of horizontal direction selectivity. The in situ hybridization experiments show that *FRMD7* expression is first detected at P3 (Figures 3B and S5). To narrow down the time window of FRMD7 function, we tested whether the lack of horizontal direction selectivity in *FRMD7^{tm}* mice is already present at eye opening. We performed microelectrode array recordings from *FRMD7^{tm}* retinas just after eye opening, at P13–P14. Whereas P13–P14 wild-type retinas had both vertical and horizontal direction-selective responses, P13–P14 retinas of *FRMD7^{tm}* mice lacked horizontal direction-selective responses, suggesting that the mechanism leading to the loss of horizontal direction selectivity operates before eye opening (Figures S4D–S4F). Thus, FRMD7 is required for the formation of horizontal direction selectivity between birth and eye opening.

The Accessory Optic System in *FRMD7^{tm}* Mice

We asked whether those on and on-off DS cells in *FRMD7^{tm}* mice that lost their horizontal direction selectivity and that normally project their axons to the NOT/DTN nuclei of the accessory optic system keep their central target. We labeled the retino-recipient areas of *FRMD7^{tm};Hoxd10-GFP* mice by injecting CTB conjugated to Alexa dye into one of the eyes. CTB is taken up by retinal ganglion cells and is transported to their axon terminals (Morin and Studholme, 2014). Subsequently, we examined the GFP-labeled axons in the retino-recipient brain areas labeled with CTB. We found that all nuclei of the accessory optic system, MTN and NOT/DTN, were innervated by GFP-positive axons, as in wild-type mice (Figure 6).

Next we mapped *FRMD7* and *ChAT* expression in the brain of P11 wild-type mice using fluorescence in situ hybridization (Figure S7A). The nuclei of the accessory optic system were labeled by injecting CTB conjugated to Alexa dye into both eyes at P8. ChAT probe was used as a landmark to identify motor nuclei. The nuclei of the accessory optic system, NOT/DTN and MTN, were negative for *FRMD7* mRNA expression. Furthermore, we did not detect *FRMD7* mRNA expression in other major visual areas, such as the lateral geniculate nucleus, primary visual cortex, and superior colliculus (data not shown). We found that *FRMD7* and *ChAT* mRNAs were co-localized in the same cells in some motor nuclei as follows: the abducens nucleus, which innervates the lateral rectus of extraocular muscles, and the oculomotor/trochlear nuclei, which innervate the other extraocular muscles (Figure S7A). Expression of *FRMD7* mRNA also was observed in the vestibulo-ocular reflex pathway, in the vestibular nuclei (Thomas et al., 2011; Figure S7A). These results suggest that FRMD7 is expressed in select cell types in the brain.

FRMD7 Is Distributed Symmetrically within Starburst Cell Processes

We examined where FRMD7 is localized within starburst cells. We performed immunohistochemistry with anti-FRMD7 and anti-ChAT antibodies on retinas at different developmental stages (P3, P5, and P7), and we examined the stained retinas using confocal microscopy (Figure 7). In neonatal stages, FRMD7 signals were present in the basal part of the cell body and processes (Figures 7A and 7B). To quantify the degree of asymmetry in the distribution of the FRMD7 signal within individual starburst cells, we determined the angle of FRMD7-labeled primary processes at P5 in whole-mount retinas (Figure 7C). We found no sign of an asymmetric FRMD7 localization, suggesting that the localization of FRMD7 is not biased to specific starburst cell processes.

FRMD7 Is Expressed in *ChAT*-Expressing Cells in the Retina of Non-human Primates

To determine whether *FRMD7* is expressed in *ChAT*-expressing cells in non-human primate retinas, we first performed immunohistochemistry with antibodies against ChAT in whole-mount retinas (Figure 8A). Similar to the findings from mice, mosaics of ChAT-labeled cells were present in both the inner nuclear and ganglion cell layers of non-human primate retinas (Rodieck and Marshak, 1992). Moreover, as in mice, the ChAT antibody labeled two retinal strata in the inner plexiform layer (Figure 8A). We then performed fluorescence in situ hybridization with antisense and control sense probes for *FRMD7* mRNA and antisense probes for *ChAT* mRNA (Figures 8B and S7B). Almost all the *ChAT*-positive cells were also positive for *FRMD7*. Conversely, a substantial fraction (70%) of *FRMD7*-positive cells in both the ganglion cell layer and inner nuclear layer were *ChAT* labeled (Figure 8C). We did not detect signals with control sense probe for *FRMD7* mRNA (Figure S7B). Thus, the mosaics of ChAT-labeled cells, and the ChAT-marked retinal strata, as

Figure 3. FRMD7 Is Specifically Expressed in Starburst Cells in the Mouse Retina

(A) Confocal images of a mouse retinal section stained by double-label quantitative fluorescence in situ hybridization using antisense probes for mouse *FRMD7* mRNA and mouse *ChAT* mRNA and DAPI. Bottom panels are magnifications of the insets in top panels.

(B) Fluorescent dots per cell for *FRMD7* mRNA (magenta) and *ChAT* mRNA (green) at different developmental stages are shown (see Figure S5A for images).

(C) Quantification of hybridization signal for control sense probe is shown (see Figure S5B for images).

(D) Confocal images show the inner nuclear layer (INL) and ganglion cell layer (GCL) of WT (left) and *FRMD7^{tm}* (right) retinas stained with anti-ChAT antibody.

(E) Quantification of the density of ChAT-positive cells from images, as given in (D), is shown.

(F) Top view of confocal images of WT (left) and *FRMD7^{tm}* (right) retinas stained with anti-ChAT antibody at the proximal (top) and distal (middle) ChAT-positive strata in the inner plexiform layer. Side view is shown at the bottom.

(G) Confocal images show starburst cells sparsely labeled with GFP-expressing rabies virus in *ChAT-Cre* mice in control (left) and *FRMD7^{tm}* (right) background.

(H) Dendritic field size (left), dendritic asymmetry index (middle), and the number of primary processes (right) of GFP-labeled starburst cells quantified from images as shown in (G). Dendritic asymmetry index refers to the ratio of length of widest diameter to that of narrowest diameter of the dendritic arbor (%).

(I) Confocal images of starburst cell processes at the proximal inner plexiform layer (IPL) sublayer labeled with synaptophysin-GFP-expressing AAV in *ChAT-Cre* mice in control (top) and *FRMD7^{tm}* (bottom) background. Data are shown as mean ± SEM; n refers to the number of retinas in (E) and cells in (C) and (H). See also Figures S1 and S5.

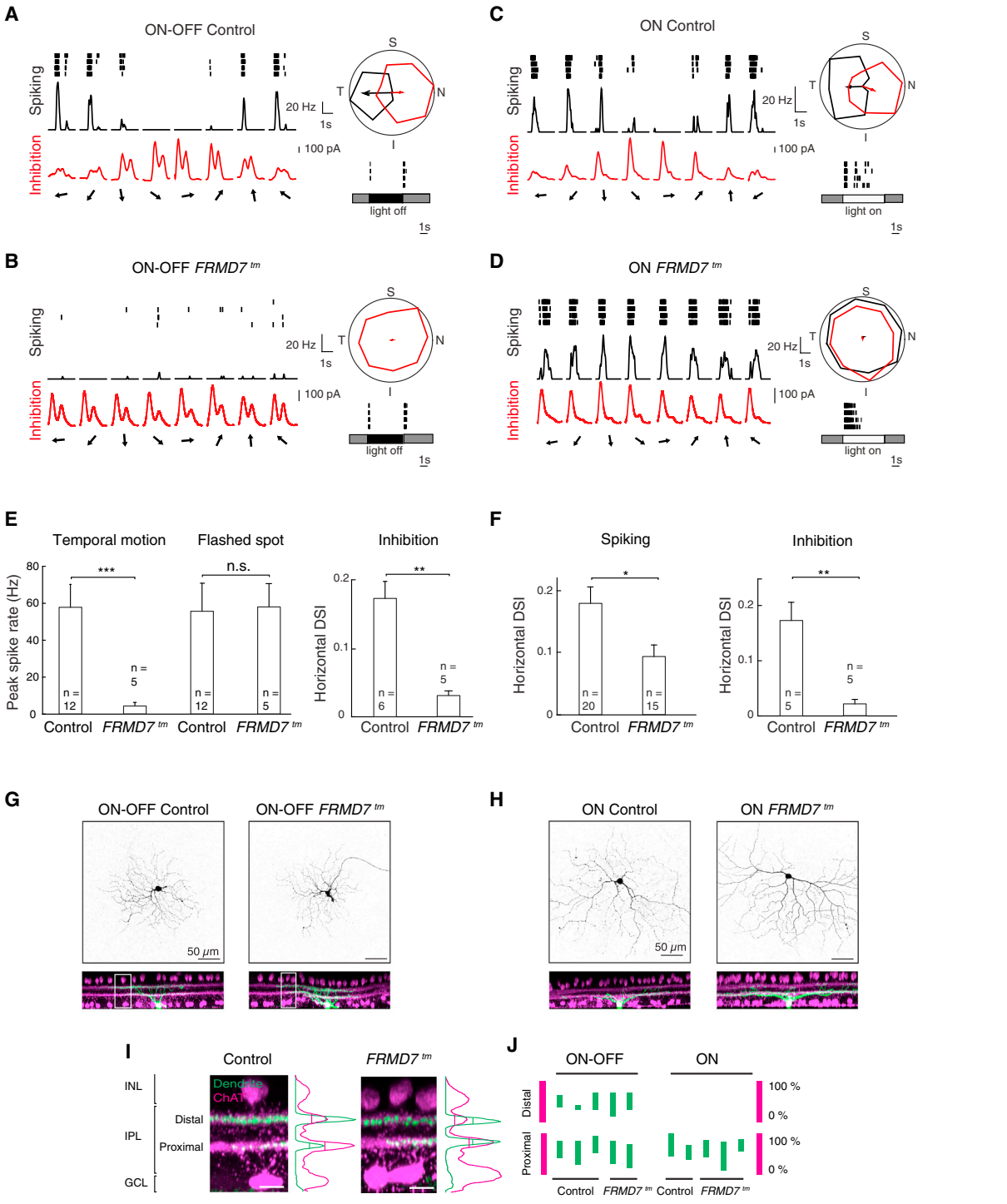

Figure 4. Ganglion Cells in *FRMD7^{tm}* Retinas with Genetic Identity of Horizontal Motion-Preferring DS Cells Lack Asymmetric Inhibitory Input

(A–D) Examples of cell-attached and whole-cell voltage-clamp recordings of GFP-labeled on-off cells (A and B) and on cells (C and D) in *Hoxd10-GFP* (Control; A and C) and *FRMD7^{tm}*;*Hoxd10-GFP* (*FRMD7^{tm}*; B and D) retinas. (Left column) Spike raster plot (black, top), spike rate (black, middle), and inhibition (red, bottom) in response to motion stimulus are shown. Arrows indicate the direction of motion. (Right column top) Polar plot of normalized (to the maximum) spike number (black) and peak inhibition (red) during motion stimulation is shown. The vector sum of spiking (black) and inhibitory (red) responses are shown by arrows. The vector sum for spikes was only plotted if the cell responded to stimulation (Supplemental Experimental Procedures). (Right column bottom) Spike raster plot in response to a 300-µm flashed-spot stimulus centered onto the cell body is shown. Gray, white, and dark areas indicate the stimulus contrast. N, nasal; T, temporal; S, superior; I, inferior.

(legend continued on next page)

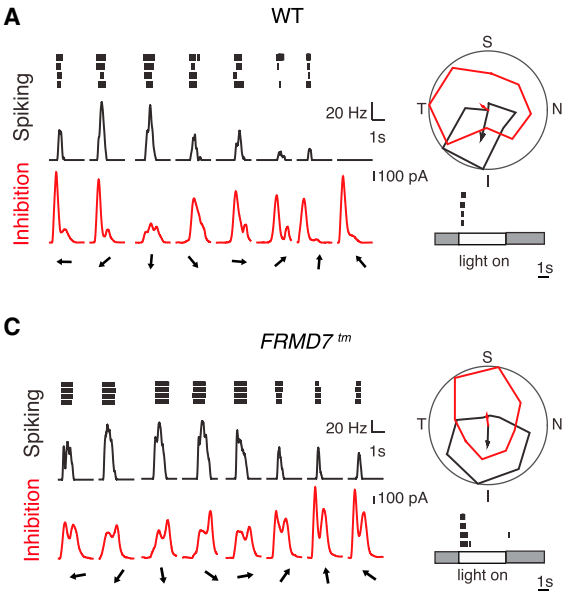

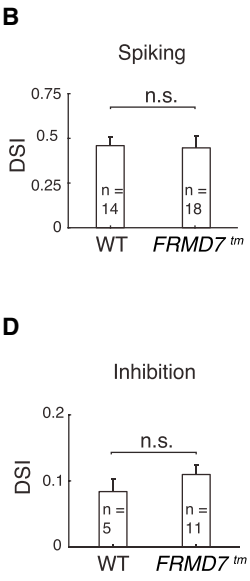

Figure 5. Vertical Direction Selectivity and Asymmetric Inhibitory Input in MTN Back-Labeled Ganglion Cells in *FRMD7^{tm}* Mice

(A and C) Examples of cell-attached and whole-cell voltage-clamp recordings of MTN back-labeled ganglion cells in WT and *FRMD7^{tm}* retinas. Spiking responses (black) and inhibitory currents (red) of vertically tuned on DS cells in WT (A) and *FRMD7^{tm}* (C) retina are shown. (Left column) Spike raster plot (black, top), spike rate (black, middle), and inhibition (red, bottom) in response to motion stimulus are shown. Arrows indicate the direction of motion. (Right column top) Polar plot of normalized (to the maximum) spike number (black) and peak inhibition (red) during motion stimulation is shown. The vector sum of spiking (black) and inhibitory (red) responses are shown by arrows. (Right column bottom) Spike raster plot in response to a 300-μm flashed-spot stimulus centered on the cell body is shown. Gray and white areas indicate the stimulus contrast.

(B and D) Bar graphs showing DSI of spiking (B) and inhibition (D) in MTN back-labeled ganglion cells in WT and *FRMD7^{tm}* retinas. Data points represent mean ± SEM; n refers to the number of recorded cells.

See also Figure S6.

well as the enrichment of *FRMD7* in *ChAT*-positive cells are conserved between mice and non-human primates.

DISCUSSION

We found that *FRMD7*, a gene responsible for 70% of cases of idiopathic congenital nystagmus in humans, is required in the mouse retina to establish spatially asymmetric inhibitory inputs from starburst cells to DS cells along the horizontal axis, and is thus required for horizontal direction selectivity. The retinal expression of *FRMD7* is restricted to starburst cells in mice and enriched in *ChAT*-labeled cells in primates. Vertical direction selectivity was not dependent on *FRMD7*. Similar to results in humans, the dysfunction of FRMD7 in mice leads to the loss of the horizontal optokinetic reflex. These results establish *FRMD7* as a member of a previously unidentified molecular pathway that is necessary for the establishment of neuronal circuit asymmetries.

Circuit Mechanism Underlying the Lack of Horizontal Direction Selectivity in *FRMD7^{tm}* Mouse Retina

We suggest that the lack of horizontal direction selectivity in the retina of *FRMD7^{tm}* mice is due to the lack of asymmetric connectivity between starburst cells and ganglion cells with the genetic identity of wild-type horizontal motion-preferring DS cells. The following set of evidence supports this conclusion. First, *FRMD7* was only expressed in *ChAT*-labeled cells (Figures 3A, 3B, 7, and S5), and ChAT is a selective marker of starburst cells in mice (Ivanova et al., 2010). Second, we found symmetric inhibitory currents in GFP-labeled on-off cells in the *FRMD7^{tm}* background in a mouse line in which, in the wild-type background, all GFP-labeled on-off cells are DS cells preferring horizontal motion (Figures 4 and S6). Third, vertical direction selectivity persisted in *FRMD7^{tm}* retinas (Figures 2 and 5). The first and second points indicate that starburst cells are the defective circuit element. The third point favors the hypothesis that, between the two key features determining asymmetric inhibition, namely the cardinal direction-organized asymmetric connectivity between starburst cell and DS cell and the centrifugal direction-organized asymmetric GABA release from starburst cell processes, it is the asymmetric connectivity between starburst cells and horizontal DS cells that is defective.

Potential Role of FRMD7 in Establishing Horizontal Asymmetric Connectivity

The results obtained are consistent with a role of FRMD7 in the reorganization of the synaptic input from starburst cells to DS cells. During the development of wild-type mice, by P6, in both on-off and on DS cells, first symmetric connections between starburst cells and DS cells are established. These symmetric connections are then reorganized to asymmetric connections before

(E) Quantification of spiking (left) and inhibitory (right) responses in on-off cells is shown.

(F) Quantification of spiking (left) and inhibitory (right) responses in on cells. In (E) and (F), data points represent mean ± SEM; n refers to the number of recorded cells (Supplemental Experimental Procedures).

(G and H) Confocal images of neurobiotin-filled, physiologically recorded on-off (G) and on (H) cells in top view (top) and side view (bottom). In side view, ChAT signals are shown (magenta) together with filled cells (green).

(I) Magnification of insets in (G). Fluorescence intensity profile for filled dendrite (green) and ChAT (magenta) along retinal depth is shown at the right of the images. Vertical lines in the profiles indicate the full width at half maximum within the IPL.

(J) Full width at half maximum of filled dendrites is shown as bars (green) relative to that of ChAT-positive proximal and distal strata (magenta).

See also Figure S6.

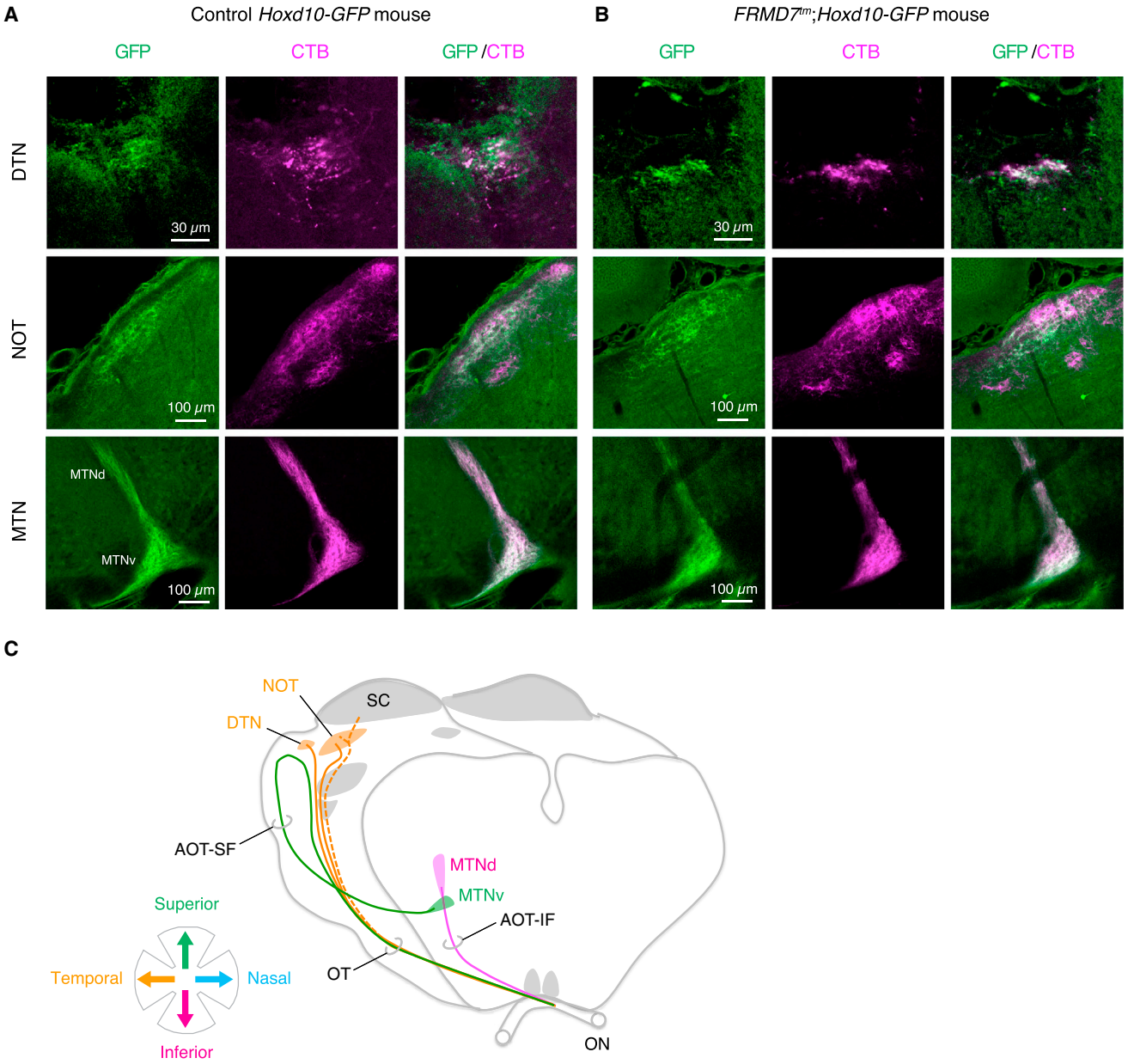

Figure 6. Hoxd10-GFP-Labeled Retinal Ganglion Cell Axons Innervate Accessory Optic Nuclei in *FRMD7^{tm}* Mice

(A and B) Confocal images show DTN (top), NOT (middle), and MTN (bottom) innervated by GFP-labeled and cholera toxin subunit B-Alexa dye conjugate (CTB)-labeled retinal ganglion cell axons in control *Hoxd10-GFP* (A) and *FRMD7^{tm}*;*Hoxd10-GFP* mice (B).

(C) Schematic of central targets of *Hox10-GFP*-labeled retinal ganglion cell axons. Axons and targets are color coded according to their directional tuning. AOT-IF, inferior fasciculus of the accessory optic tract; AOT-SF, superior fasciculus of the accessory optic tract; MTNd, dorsal division of the MTN; MTNv, ventral division of the MTN; SC, superior colliculus; ON, optic nerve; OT, optic tract. Schematic adapted from Pak et al. (1987) and Dhande et al. (2013).

See also Figure S7.

eye opening (Wei et al., 2011; Yonehara et al., 2011). Our findings suggest that, in *FRMD7^{tm}* mice, this symmetric-to-asymmetric transition is defective along the horizontal axis (Figure 8D).

How could FRMD7 contribute to the establishment of the selective connectivity between nasally or temporally pointing starburst cell processes and temporal or nasal motion-preferring DS cells? To enable the correct matching of starburst cell process and DS cell type, it is likely that nasally and temporally pointing starburst cell processes are labeled by distinct molecules or combinations of molecules. This would require a sorting machinery in the soma that knows about the horizontal directions and sends different molecules to nasally and temporally pointing processes. Since it is widely documented that the retina has a number of molecules forming nasal-temporal gradients, such as

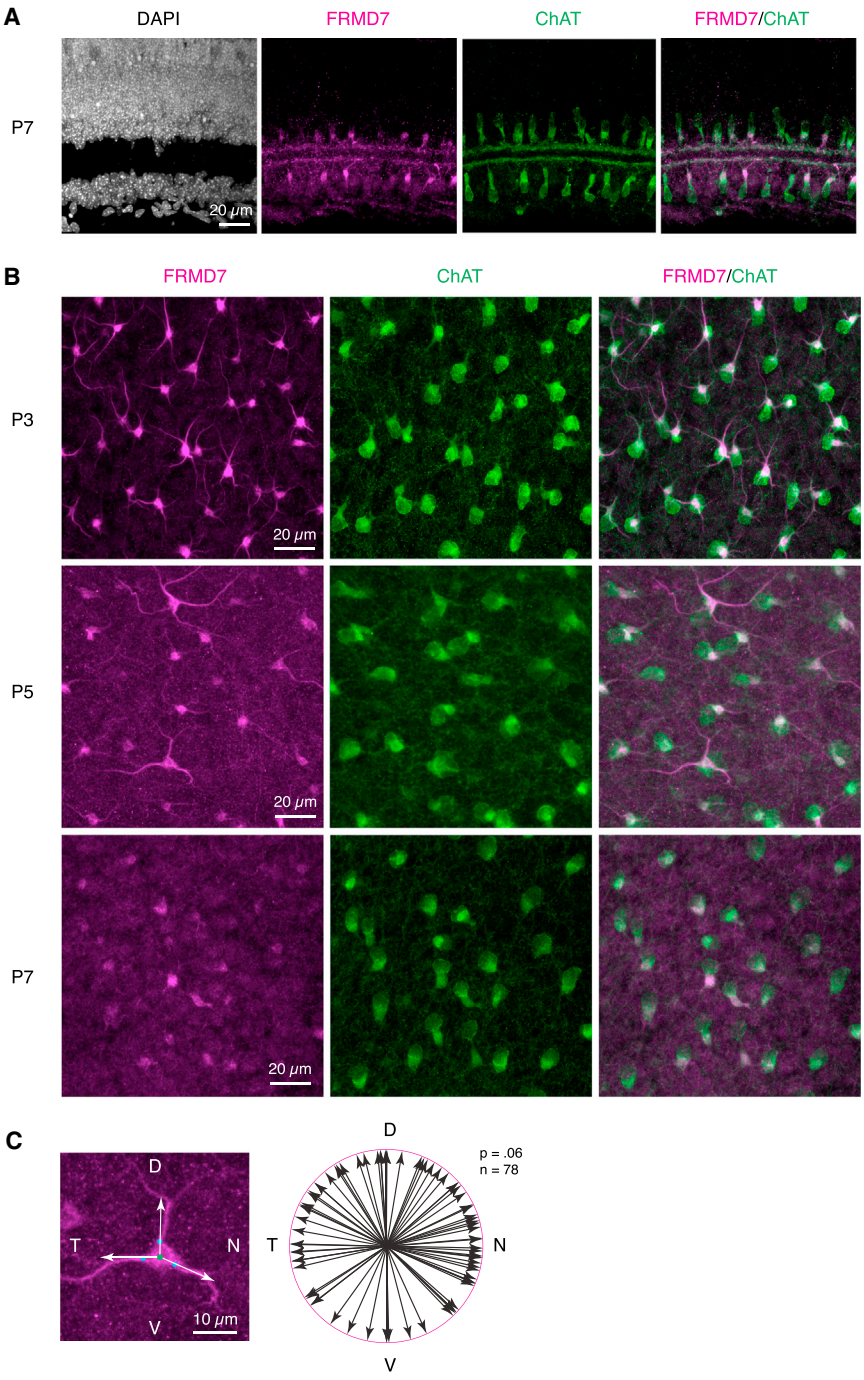

Figure 7. FRMD7 Is Symmetrically Localized within Starburst Amacrine Cell Processes

(A and B) Confocal images show WT retinas stained with antibody for ChAT (green) and FRMD7 (magenta) at different developmental time points (P3, P5, and P7) in side view (A) and top view of z stack of labeled cells in GCL (B).

(C) Quantification of the subcellular distribution of FRDM7 within starburst cells. (Left) The direction of FRMD7-labeled processes was defined by the angle of the vector, which points from the cell body center (green dot) to the exit point of the primary processes from cell body (cyan dots). (Right) Distribution of the direction of FRMD7-labeled processes is shown.

ephrins and BMPs (Sakuta et al., 2006), it is likely that the knowledge of starburst cells about the opposing horizontal directions is learned from these gradients. Along the vertical axis a similar differential sorting mechanism may label superiorly and inferiorly pointing starburst cell processes. The findings that both nasal and temporal direction selectivities are abolished in *FRMD7^{tm}* mice (Figures 2 and S4) and that FRMD7 protein was found symmetrically distributed in the processes of starburst cells (Figures 7B and 7C) suggest that FRMD7 is not a marker for nasal or temporal processes. It is more likely that FRMD7 is part of the molecular machinery that is either involved in sensing or sorting along the horizontal axis.

While it is an open question where and how FRMD7 exerts its function in the starburst cell to establish asymmetric connectivity, the organization of the protein and the precise location of the mutations found in individuals with congenital nystagmus provide insights. The *FRMD7* gene encodes a member of the FERM domain family of proteins (Moleirinho et al., 2013). The FERM domain of FRMD7 is located in the N terminus and is thought to link FRMD7 to the cell membrane. Next to the FERM domain is a FERM-adjacent domain, which in other FERM-containing proteins is thought to be subject to phosphorylation. Notably, the mutations causing congenital nystagmus in humans are concentrated in the FERM domain and a region around the FERM-adjacent domain (Thomas et al., 2011). The C-terminal part of FRMD7 has no homology with other proteins. Other FERM domain-containing proteins are involved in the signal transduction between the plasma membrane and the actin cytoskeleton (Moleirinho et al., 2013). Indeed, the FRMD7 protein interacts with the Rho GDP-dissociation inhibitor alpha, the main regulator of Rho GDPases, which are key regulators of the reorganization of actin cytoskeleton (Pu et al., 2013). These findings raise the possibility that FRMD7 also signals between the plasma membrane and the cytoskeleton.

Circuit Mechanism Underlying the Lack of the Horizontal Optokinetic Reflex in *FRMD7^{tm}* Mice

We propose that the lack of horizontal direction selectivity in the retina contributes significantly to the lack of the horizontal

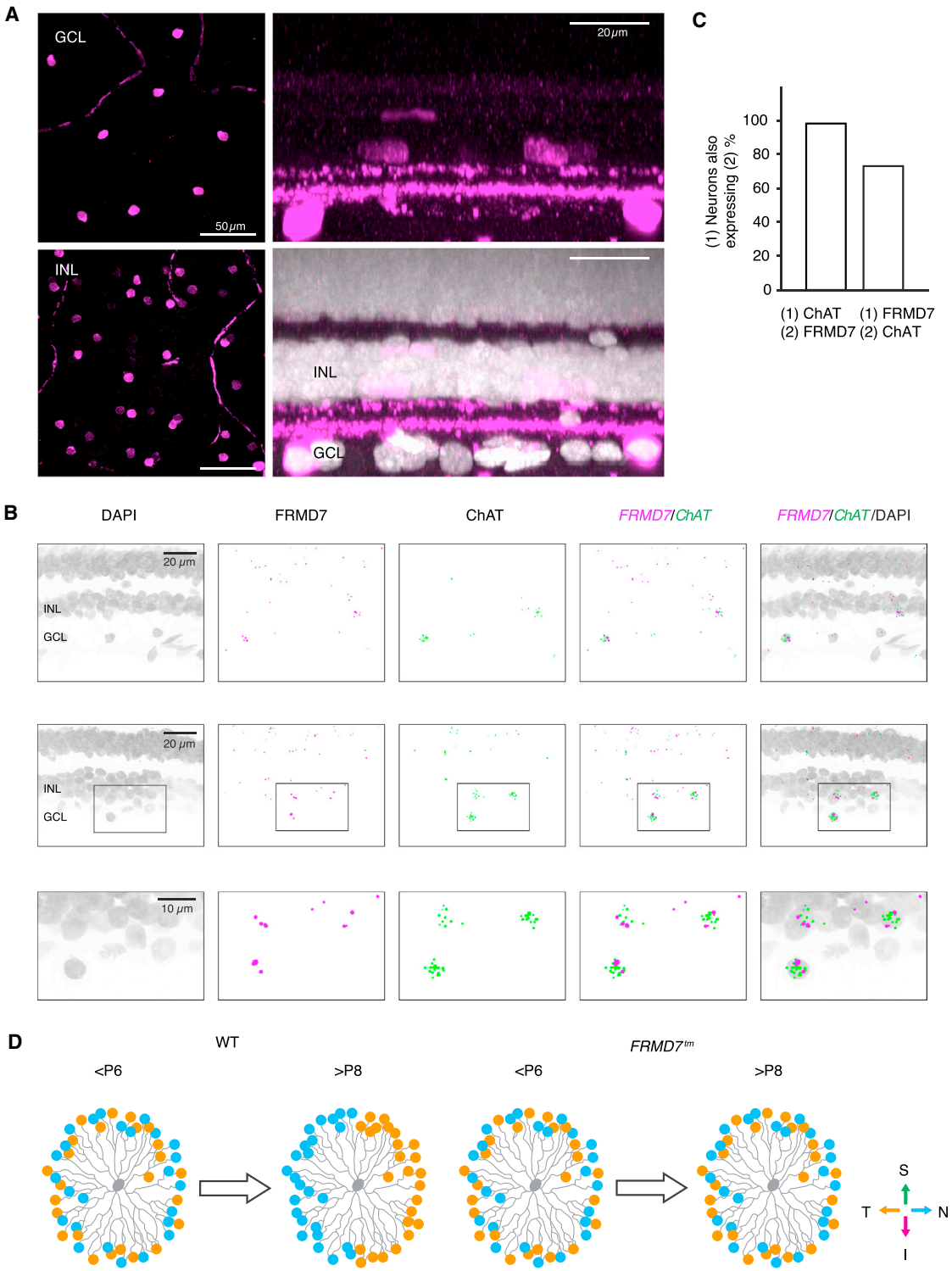

Figure 8. FRMD7 Is Expressed in ChAT-Labeled Cells in the Retina of Non-human Primates

(A) Confocal images show whole-mount non-human primate retinas stained with antibody for ChAT (magenta) and DAPI (white) in top view (left) and side view (right).

(B) Confocal images of retinal sections stained by double-label fluorescence in situ hybridization using antisense probes for *FRMD7* mRNA and *ChAT* mRNA as well as DAPI in non-human primate retinas. Two example regions (top and middle) and magnification of inset in middle panels (bottom) are shown.

(C) Relationship between *FRMD7* mRNA-expressing and *ChAT* mRNA-expressing cells is shown.

(legend continued on next page)

optokinetic reflex in *FRMD7^{tm}* mice. The following evidence supports this conclusion. First, it has been shown previously that mice whose retinal direction selectivity has been abolished by the genetic ablation of starburst cells lose the optokinetic reflex (Yoshida et al., 2001). In that study, the genetic manipulation was done in the retina alone, without affecting any circuits in the brain. Second, it has been shown in cats that activity in the NOT/DTN complex, which processes horizontal direction-selective input, is required selectively for the horizontal optokinetic reflex (Hoffmann and Fischer, 2001). Third, we found that the defective DS cells in *FRMD7^{tm}* mice project to their normal brain targets (Figure 6). Fourth, *FRMD7^{tm}* mice were able to produce spontaneous, large-amplitude horizontal eye motions (Figures 1F and 1G). Fifth, *FRMD7^{tm}* mice had normal vertical retinal direction selectivity (Figures 2 and 5) and showed a normal vertical optokinetic reflex (Figure 1E). Sixth, the optokinetic reflex was measured in head-fixed mice, limiting possible interactions with the vestibular system. Taken together, these results suggest that the lack of horizontal direction selectivity in the retina is sufficient to abolish the horizontal optokinetic reflex. However, as we detected *FRMD7* mRNA expression in the motor nuclei responsible for eye movements and in the vestibular nuclei (Figure S7A), we cannot rule out contributions to the defective optokinetic response from motor and vestibular nuclei.

Circuit Mechanism Underlying the Symptoms of FRMD7-Based Idiopathic Congenital Nystagmus in Humans

Can FRMD7 dysfunction in starburst cells be a contributor to, or cause of, the lack of horizontal optokinetic reflex in FRMD7-based congenital nystagmus in humans? The following findings support this interpretation. First, the neuronal pathways controlling the optokinetic reflex are highly conserved across mammals. Although on DS cells have not yet been recorded in primate retinas, on direction-selective cells preferring the ipsiversive direction (i.e., left NOT/DTN is activated by the leftward motion and vice versa) have been recorded in primate NOT/DTN brain areas (Distler and Hoffmann, 2011; Hoffmann, 1989), which are the targets of horizontal on DS cells in other animals (Dhande et al., 2013). Second, in adult non-human primate retinas, the same ChAT antibody, which in mice labels two mosaics of starburst cells and two retinal strata in the inner plexiform layer where the processes of starburst cells ramify, also labeled two mosaics of cells in the same nuclear layers and two retina strata in the inner plexiform layer (Rodieck and Marshak, 1992; Figure 8A). Third, *FRMD7* was expressed in those non-human primate retinal cells that were marked by *ChAT* (Figures 8B and 8C). Fourth, we show that human subjects with congenital nystagmus were able to produce voluntary, smooth-pursuit, horizontal eye movements (Figures 1K and 1L). Fifth, the vertical optokinetic reflex is still present in individuals with congenital nystagmus (Figure 1J). Taken together, this evidence indicates that, in primates, *FRMD7* is expressed in a retinal cell population that has the morphological and genetic attributes of starburst cells in mice and that the motor system controlling horizontal eye movements in individuals with congenital nystagmus is functional. These findings are consistent with a hypothesis that the loss of the horizontal optokinetic reflex in humans is, at least partly, due to the loss of FRMD7 function in starburst cells. Note that, in humans, *FRMD7* mRNA expression also has been observed in the brain regions involved in vestibulo-ocular reflex (Tarpey et al., 2006; Thomas et al., 2011). However, since the optokinetic reflex was assessed in head-fixed human subjects, a potential dysfunction in the vestibular system is unlikely to fully explain the loss of the horizontal optokinetic reflex.

In contrast to individuals with FRMD7-based nystagmus, we did not observe spontaneous oscillatory eye movements (nystagmus) in *FRMD7^{tm}* mice. This lack can be explained in at least two different ways. First, it is possible that the presence of horizontal nystagmus is linked to the lack of the horizontal optokinetic reflex in humans. For example, an inhibitory interaction between the control circuits generating the optokinetic reflex and microsaccades in humans (Otero-Millan et al., 2011) may exist. When the horizontal optokinetic reflex is lost, inhibition decreases and horizontal microsaccades become larger and uncontrolled, appearing as horizontal nystagmus. As wild-type mice are not confirmed to have microsaccades, the absence of this type of eye movement may explain why there is no nystagmus in *FRMD7^{tm}* mice. Alternatively, the two symptoms, nystagmus and the lack of the horizontal optokinetic reflex, could be caused by two independent circuit mechanisms. Indeed, the presence of horizontal nystagmus together with a normal optokinetic reflex in achromatopsia shows that the two symptoms can be independent of each other (Yee et al., 1981). It is possible that a defect in the connectivity between starburst cells and DS cells leads to the lack of the horizontal optokinetic reflex, and, independently, either a defect in the retinal fovea (Thomas et al., 2014), which is absent in mouse retinas, or a dysfunction of another brain circuit causes nystagmus.

EXPERIMENTAL PROCEDURES

Animal and Human Subjects

The study protocols for animals and humans were approved by the relevant Institutional Review Boards.

Further description of the experimental procedures is provided in the Supplemental Experimental Procedures.

SUPPLEMENTAL INFORMATION

Supplemental Information includes Supplemental Experimental Procedures, seven figures, and one movie and can be found with this article online at http://dx.doi.org/10.1016/j.neuron.2015.11.032.

AUTHOR CONTRIBUTIONS

K.Y. designed experiments; performed retinal experiments, in vivo injections, and in situ hybridization; grew rabies virus; developed all plasmids; analyzed

(D) Schematic of the development of horizontal asymmetric inhibitory outputs of a starburst cell (gray, center) in WT (left) and *FRMD7^{tm}* mice (right) during the postnatal period before eye opening. Output inhibitory synapses are color coded according to the preferred directions (colored arrows) of the postsynaptic DS cell partner. Symmetric inhibitory connectivity established during the first postnatal week is reorganized into asymmetric inhibitory connectivity during the second postnatal week in WT mice (Wei et al., 2011; Yonehara et al., 2011), but not in *FRMD7^{tm}* mice.

data; and wrote the paper. M.F. performed microelectrode array recordings, analyzed data, and wrote the paper. A.D. performed patch-clamp recordings, analyzed data, and wrote the paper. F.E. performed human eye movement recordings, analyzed data, and helped write the paper. S.T. performed human and mouse eye movement recordings, analyzed data, and helped write the paper. J.K. performed *FRMD7* mRNA analysis. F.F. developed software for microelectrode array data analysis and analyzed data. B.G.S. performed in situ hybridization and immunohistochemistry. A.K. selected patients and helped with human eye movement recordings. J.M. built the microelectrode array recording system and setup. A.S. helped with histology. J.J. made AAV viruses. F.C. helped with primate tissue collection. A.P.R made AAV constructs. J.N., Z.Z.N., and F.M. selected and diagnosed patients. A.H. designed and supervised microelectrode array recordings and technology developments. B.R. designed experiments, analyzed data, and wrote the paper.

ACKNOWLEDGMENTS

We thank Nathalie Stuber, Reto Baumgartner, Tamas Szikra, Zoltan Raics, Monique Lerch, Sabrina Djaffer, and Claudia Patricia Patiño Alvarez for technical support and Sara Oakeley for commenting on the manuscript. We acknowledge the following grants: Boehringer Ingelheim Fonds PhD fellowship to A.D.; Japan Society for the Promotion of Science Postdoctoral Fellowship for Research Abroad, Lundbeck Foundation, and European Research Council Starting Grant "CIRCUITASSEMBLY" to K.Y.; Human Frontier Science Program Postdoctoral Fellowship LT000173/2013 to S.T.; Gebert-Rüf Foundation, Swiss National Science Foundation, European Research Council, National Centres of Competence in Research Molecular Systems Engineering, Swiss National Science Foundation Sinergia, Swiss-Hungarian, and European Union 3X3D Imaging grants to B.R. The ETH Zurich group, M.F., F.F., J. M., and A.H. acknowledge funding through the European Research Council Advanced Grant "NeuroCMOS," contract AdG 267351, and the Swiss National Science Foundation Sinergia Project CRSII3_141801.

Received: July 6, 2015
Revised: August 14, 2015
Accepted: November 18, 2015
Published: December 17, 2015

REFERENCES

Borst, A., and Euler, T. (2011). Seeing things in motion: models, circuits, and mechanisms. Neuron *71*, 974–994.

Borst, A., and Helmstaedter, M. (2015). Common circuit design in fly and mammalian motion vision. Nat. Neurosci. *18*, 1067–1076.

Briggman, K.L., Helmstaedter, M., and Denk, W. (2011). Wiring specificity in the direction-selectivity circuit of the retina. Nature *471*, 183–188.

Bryan, A.S., and Angelaki, D.E. (2009). Optokinetic and vestibular responsiveness in the macaque rostral vestibular and fastigial nuclei. J. Neurophysiol. *101*, 714–720.

Dhande, O.S., Estevez, M.E., Quattrochi, L.E., El-Danaf, R.N., Nguyen, P.L., Berson, D.M., and Huberman, A.D. (2013). Genetic dissection of retinal inputs to brainstem nuclei controlling image stabilization. J. Neurosci. *33*, 17797–17813.

Distler, C., and Hoffmann, K.-P. (2011). Visual pathway for the optokinetic reflex in infant macaque monkeys. J. Neurosci. *31*, 17659–17668.

Duan, X., Krishnaswamy, A., De la Huerta, I., and Sanes, J.R. (2014). Type II cadherins guide assembly of a direction-selective retinal circuit. Cell *158*, 793–807.

Elstrott, J., Anishchenko, A., Greschner, M., Sher, A., Litke, A.M., Chichilnisky, E.J., and Feller, M.B. (2008). Direction selectivity in the retina is established independent of visual experience and cholinergic retinal waves. Neuron *58*, 499–506.

Euler, T., Detwiler, P.B., and Denk, W. (2002). Directionally selective calcium signals in dendrites of starburst amacrine cells. Nature *418*, 845–852.

Famiglietti, E.V. (1991). Synaptic organization of starburst amacrine cells in rabbit retina: analysis of serial thin sections by electron microscopy and graphic reconstruction. J. Comp. Neurol. *309*, 40–70.

Faulstich, B.M., Onori, K.A., and du Lac, S. (2004). Comparison of plasticity and development of mouse optokinetic and vestibulo-ocular reflexes suggests differential gain control mechanisms. Vision Res. *44*, 3419–3427.

Fried, S.I., Münch, T.A., and Werblin, F.S. (2002). Mechanisms and circuitry underlying directional selectivity in the retina. Nature *420*, 411–414.

Gauvain, G., and Murphy, G.J. (2015). Projection-specific characteristics of retinal input to the brain. J. Neurosci. *35*, 6575–6583.

Gavrikov, K.E., Dmitriev, A.V., Keyser, K.T., and Mangel, S.C. (2003). Cation–chloride cotransporters mediate neural computation in the retina. Proc. Natl. Acad. Sci. USA *100*, 16047–16052.

Giolli, R.A., Blanks, R.H.I., and Lui, F. (2006). The accessory optic system: basic organization with an update on connectivity, neurochemistry, and function. Prog. Brain Res. *151*, 407–440.

Gottlob, I., and Proudlock, F.A. (2014). Aetiology of infantile nystagmus. Curr. Opin. Neurol. *27*, 83–91.

Hausselt, S.E., Euler, T., Detwiler, P.B., and Denk, W. (2007). A dendrite-autonomous mechanism for direction selectivity in retinal starburst amacrine cells. PLoS Biol. *5*, e185.

Hoffmann, K.P. (1989). Control of the optokinetic reflex by the nucleus of the optic tract in primates. Prog. Brain Res. *80*, 173–182, discussion 171–172.

Hoffmann, K.P., and Fischer, W.H. (2001). Directional effect of inactivation of the nucleus of the optic tract on optokinetic nystagmus in the cat. Vision Res. *41*, 3389–3398.

Ivanova, E., Hwang, G.-S., and Pan, Z.-H. (2010). Characterization of transgenic mouse lines expressing Cre recombinase in the retina. Neuroscience *165*, 233–243.

Kay, J.N., De la Huerta, I., Kim, I.-J., Zhang, Y., Yamagata, M., Chu, M.W., Meister, M., and Sanes, J.R. (2011). Retinal ganglion cells with distinct directional preferences differ in molecular identity, structure, and central projections. J. Neurosci. *31*, 7753–7762.

Kim, I.-J., Zhang, Y., Yamagata, M., Meister, M., and Sanes, J.R. (2008). Molecular identification of a retinal cell type that responds to upward motion. Nature *452*, 478–482.

Kim, J.S., Greene, M.J., Zlateski, A., Lee, K., Richardson, M., Turaga, S.C., Purcaro, M., Balkam, M., Robinson, A., Behabadi, B.F., et al.; EyeWirers (2014). Space-time wiring specificity supports direction selectivity in the retina. Nature *509*, 331–336.

Lee, S., and Zhou, Z.J. (2006). The synaptic mechanism of direction selectivity in distal processes of starburst amacrine cells. Neuron *51*, 787–799.

Lee, S., Kim, K., and Zhou, Z.J. (2010). Role of ACh-GABA cotransmission in detecting image motion and motion direction. Neuron *68*, 1159–1172.

Miyamichi, K., Shlomai-Fuchs, Y., Shu, M., Weissbourd, B.C., Luo, L., and Mizrahi, A. (2013). Dissecting local circuits: parvalbumin interneurons underlie broad feedback control of olfactory bulb output. Neuron *80*, 1232–1245.

Moleirinho, S., Tilston-Lunel, A., Angus, L., Gunn-Moore, F., and Reynolds, P.A. (2013). The expanding family of FERM proteins. Biochem. J. *452*, 183–193.

Morin, L.P., and Studholme, K.M. (2014). Retinofugal projections in the mouse. J. Comp. Neurol. *522*, 3733–3753.

Oesch, N., Euler, T., and Taylor, W.R. (2005). Direction-selective dendritic action potentials in rabbit retina. Neuron *47*, 739–750.

Osterhout, J.A., Stafford, B.K., Nguyen, P.L., Yoshihara, Y., and Huberman, A.D. (2015). Contactin-4 mediates axon-target specificity and functional development of the accessory optic system. Neuron *86*, 985–999.

Otero-Millan, J., Macknik, S.L., Serra, A., Leigh, R.J., and Martinez-Conde, S. (2011). Triggering mechanisms in microsaccade and saccade generation: a novel proposal. Ann. N Y Acad. Sci. *1233*, 107–116.

Oyster, C.W., Takahashi, E., and Collewijn, H. (1972). Direction-selective retinal ganglion cells and control of optokinetic nystagmus in the rabbit. Vision Res. *12*, 183–193.

Pak, M.W., Giolli, R.A., Pinto, L.H., Mangini, N.J., Gregory, K.M., and Vanable, J.W., Jr. (1987). Retinopretectal and accessory optic projections of normal mice and the OKN-defective mutant mice beige, beige-J, and pearl. J. Comp. Neurol. *258*, 435–446.

Pei, Z., Chen, Q., Koren, D., Giammarinaro, B., Acaron Ledesma, H., and Wei, W. (2015). Conditional Knock-Out of Vesicular GABA Transporter Gene from Starburst Amacrine Cells Reveals the Contributions of Multiple Synaptic Mechanisms Underlying Direction Selectivity in the Retina. J. Neurosci. *35*, 13219–13232.

Pu, J., Mao, Y., Lei, X., Yan, Y., Lu, X., Tian, J., Yin, X., Zhao, G., and Zhang, B. (2013). FERM domain containing protein 7 interacts with the Rho GDP dissociation inhibitor and specifically activates Rac1 signaling. PLoS ONE *8*, e73108.

Rodieck, R.W., and Marshak, D.W. (1992). Spatial density and distribution of choline acetyltransferase immunoreactive cells in human, macaque, and baboon retinas. J. Comp. Neurol. *321*, 46–64.

Sakuta, H., Takahashi, H., Shintani, T., Etani, K., Aoshima, A., and Noda, M. (2006). Role of bone morphogenic protein 2 in retinal patterning and retinotectal projection. J. Neurosci. *26*, 10868–10878.

Sanes, J.R., and Masland, R.H. (2015). The types of retinal ganglion cells: current status and implications for neuronal classification. Annu. Rev. Neurosci. *38*, 221–246.

Schweigart, G., Mergner, T., Evdokimidis, I., Morand, S., and Becker, W. (1997). Gaze stabilization by optokinetic reflex (OKR) and vestibulo-ocular reflex (VOR) during active head rotation in man. Vision Res. *37*, 1643–1652.

Siegert, S., Cabuy, E., Scherf, B.G., Kohler, H., Panda, S., Le, Y.-Z., Fehling, H.J., Gaidatzis, D., Stadler, M.B., and Roska, B. (2012). Transcriptional code and disease map for adult retinal cell types. Nat. Neurosci. *15*, 487–495.

Simpson, J.I. (1984). The accessory optic system. Annu. Rev. Neurosci. *7*, 13–41.

Sivyer, B., and Williams, S.R. (2013). Direction selectivity is computed by active dendritic integration in retinal ganglion cells. Nat. Neurosci. *16*, 1848–1856.

Soodak, R.E., and Simpson, J.I. (1988). The accessory optic system of rabbit. I. Basic visual response properties. J. Neurophysiol. *60*, 2037–2054.

Stacy, R.C., and Wong, R.O.L. (2003). Developmental relationship between cholinergic amacrine cell processes and ganglion cell dendrites of the mouse retina. J. Comp. Neurol. *456*, 154–166.

Sun, L.O., Jiang, Z., Rivlin-Etzion, M., Hand, R., Brady, C.M., Matsuoka, R.L., Yau, K.-W., Feller, M.B., and Kolodkin, A.L. (2013). On and off retinal circuit assembly by divergent molecular mechanisms. Science *342*, 1241974.

Sun, L.O., Brady, C.M., Cahill, H., Al-Khindi, T., Sakuta, H., Dhande, O.S., Noda, M., Huberman, A.D., Nathans, J., and Kolodkin, A.L. (2015). Functional assembly of accessory optic system circuitry critical for compensatory eye movements. Neuron *86*, 971–984.

Tarpey, P., Thomas, S., Sarvananthan, N., Mallya, U., Lisgo, S., Talbot, C.J., Roberts, E.O., Awan, M., Surendran, M., McLean, R.J., et al. (2006). Mutations in FRMD7, a newly identified member of the FERM family, cause X-linked idiopathic congenital nystagmus. Nat. Genet. *38*, 1242–1244.

Thomas, S., Proudlock, F.A., Sarvananthan, N., Roberts, E.O., Awan, M., McLean, R., Surendran, M., Kumar, A.S.A., Farooq, S.J., Degg, C., et al. (2008). Phenotypical characteristics of idiopathic infantile nystagmus with and without mutations in FRMD7. Brain *131*, 1259–1267.

Thomas, M.G., Crosier, M., Lindsay, S., Kumar, A., Thomas, S., Araki, M., Talbot, C.J., McLean, R.J., Surendran, M., Taylor, K., et al. (2011). The clinical and molecular genetic features of idiopathic infantile periodic alternating nystagmus. Brain *134*, 892–902.

Thomas, M.G., Crosier, M., Lindsay, S., Kumar, A., Araki, M., Leroy, B.P., McLean, R.J., Sheth, V., Maconachie, G., Thomas, S., et al. (2014). Abnormal retinal development associated with FRMD7 mutations. Hum. Mol. Genet. *23*, 4086–4093.

Trenholm, S., Johnson, K., Li, X., Smith, R.G., and Awatramani, G.B. (2011). Parallel mechanisms encode direction in the retina. Neuron *71*, 683–694.

Trenholm, S., McLaughlin, A.J., Schwab, D.J., Turner, M.H., Smith, R.G., Rieke, F., and Awatramani, G.B. (2014). Nonlinear dendritic integration of electrical and chemical synaptic inputs drives fine-scale correlations. Nat. Neurosci. *17*, 1759–1766.

van Alphen, A.M., Stahl, J.S., and De Zeeuw, C.I. (2001). The dynamic characteristics of the mouse horizontal vestibulo-ocular and optokinetic response. Brain Res. *890*, 296–305.

Vaney, D.I., Sivyer, B., and Taylor, W.R. (2012). Direction selectivity in the retina: symmetry and asymmetry in structure and function. Nat. Rev. Neurosci. *13*, 194–208.

Wei, W., and Feller, M.B. (2011). Organization and development of direction-selective circuits in the retina. Trends Neurosci. *34*, 638–645.

Wei, W., Hamby, A.M., Zhou, K., and Feller, M.B. (2011). Development of asymmetric inhibition underlying direction selectivity in the retina. Nature *469*, 402–406.

Yee, R.D., Baloh, R.W., and Honrubia, V. (1981). Eye movement abnormalities in rod monochromacy. Ophthalmology *88*, 1010–1018.

Yonehara, K., Ishikane, H., Sakuta, H., Shintani, T., Nakamura-Yonehara, K., Kamiji, N.L., Usui, S., and Noda, M. (2009). Identification of retinal ganglion cells and their projections involved in central transmission of information about upward and downward image motion. PLoS ONE *4*, e4320.

Yonehara, K., Balint, K., Noda, M., Nagel, G., Bamberg, E., and Roska, B. (2011). Spatially asymmetric reorganization of inhibition establishes a motion-sensitive circuit. Nature *469*, 407–410.

Yonehara, K., Farrow, K., Ghanem, A., Hillier, D., Balint, K., Teixeira, M., Jüttner, J., Noda, M., Neve, R.L., Conzelmann, K.-K., and Roska, B. (2013). The first stage of cardinal direction selectivity is localized to the dendrites of retinal ganglion cells. Neuron *79*, 1078–1085.

Yoshida, K., Watanabe, D., Ishikane, H., Tachibana, M., Pastan, I., and Nakanishi, S. (2001). A key role of starburst amacrine cells in originating retinal directional selectivity and optokinetic eye movement. Neuron *30*, 771–780.

Neuron

Supplemental Information

Congenital Nystagmus Gene FRMD7 Is Necessary for Establishing a Neuronal Circuit Asymmetry for Direction Selectivity

Keisuke Yonehara, Michele Fiscella, Antonia Drinnenberg, Federico Esposti, Stuart Trenholm, Jacek Krol, Felix Franke, Brigitte Gross Scherf, Akos Kusnyerik, Jan Müller, Arnold Szabo, Josephine Jüttner, Francisco Cordoba, Ashrithpal Police Reddy, János Németh, Zoltán Zsolt Nagy, Francis Munier, Andreas Hierlemann, and Botond Roska

Figure S1

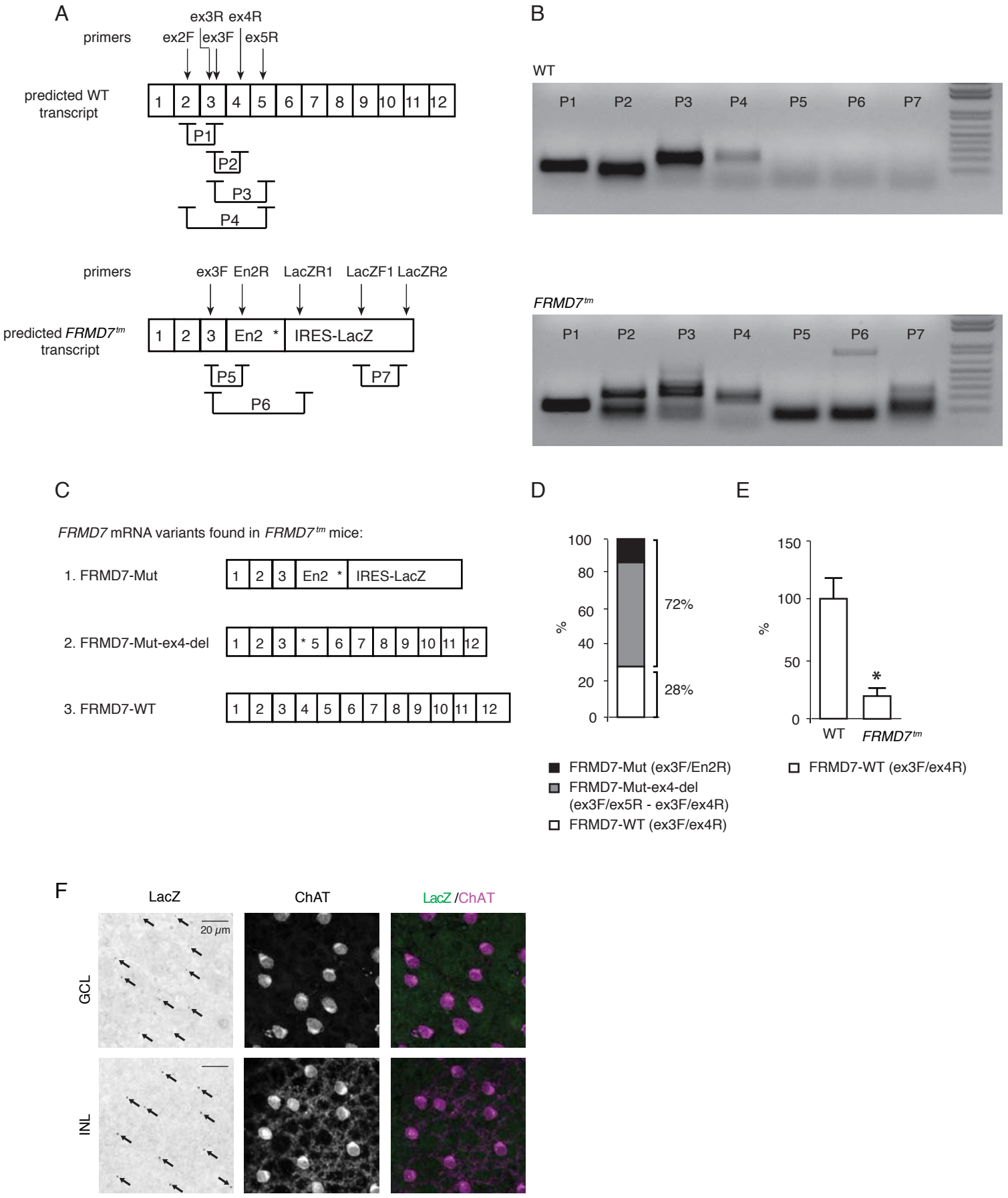
A
primers
ex3R ex4R
ex2F ex3F ex5R
predicted WT transcript
1 2 3 4 5 6 7 8 9 10 11 12
P1
P2
P3
P4
primers
ex3F En2R LacZR1 LacZF1 LacZR2
predicted FRMD7tm transcript
1 2 3 En2 * IRES-LacZ
P5
P7
P6
B
WT
P1 P2 P3 P4 P5 P6 P7
FRMD7tm
P1 P2 P3 P4 P5 P6 P7
C
FRMD7 mRNA variants found in FRMD7tm mice:
1. FRMD7-Mut
1 2 3 En2 * IRES-LacZ
2. FRMD7-Mut-ex4-del
1 2 3 * 5 6 7 8 9 10 11 12
3. FRMD7-WT
1 2 3 4 5 6 7 8 9 10 11 12
D
100
80
60
40
20
0
%
72%
28%
FRMD7-Mut (ex3F/En2R)
FRMD7-Mut-ex4-del (ex3F/ex5R - ex3F/ex4R)
FRMD7-WT (ex3F/ex4R)
E
150
100
50
0
%
*
WT
FRMD7tm
FRMD7-WT (ex3F/ex4R)
F
LacZ
ChAT
LacZ /ChAT
20 μm
GCL
INL

Figure S2

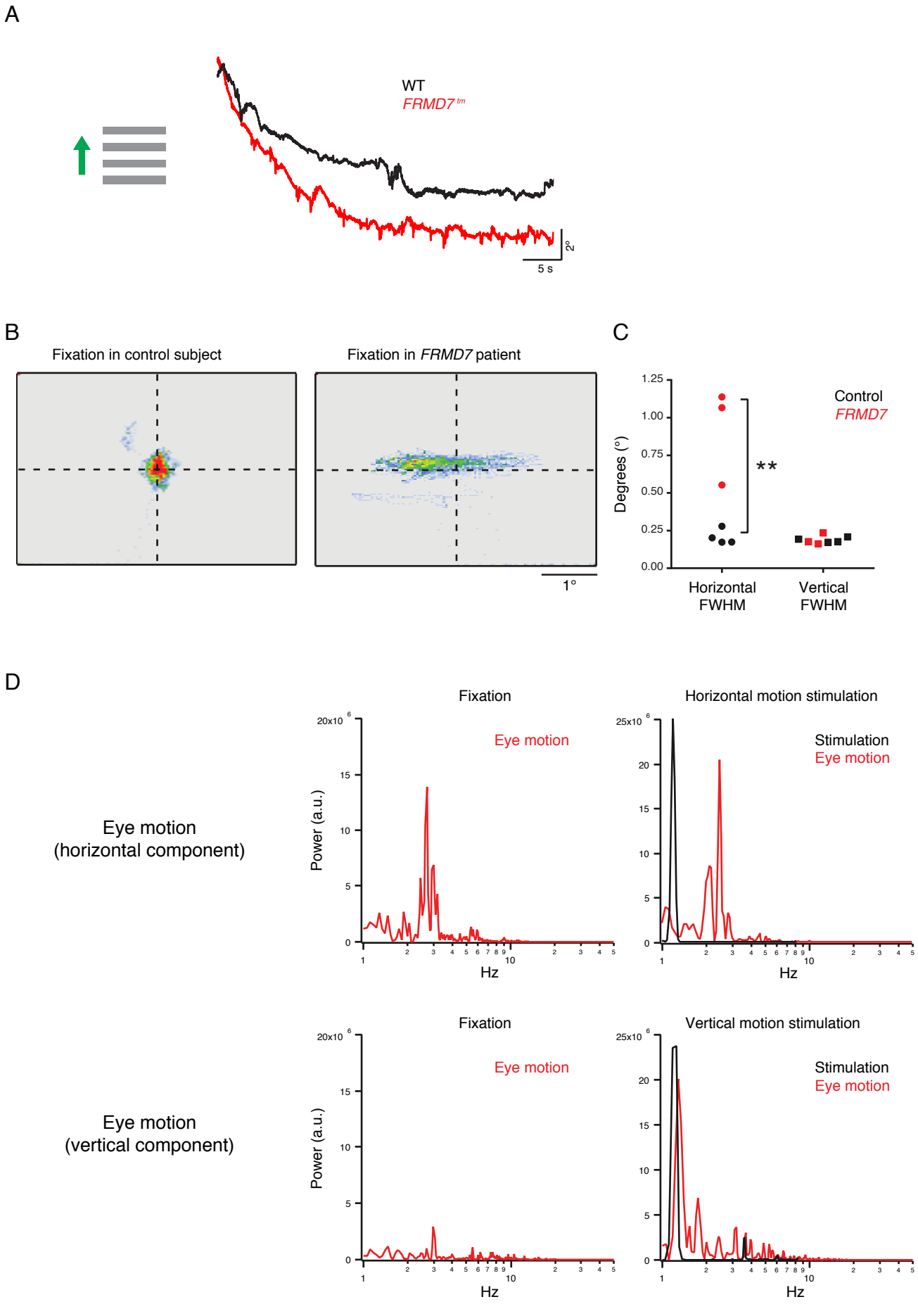
A
WT
FRMD7 tm
2°
5 s
B
Fixation in control subject
Fixation in FRMD7 patient
1°
C
Control
FRMD7
Degrees (°)
1.25
1.00
0.75
0.50
0.25
0.00
**
Horizontal FWHM
Vertical FWHM
D
Eye motion (horizontal component)
Fixation
Horizontal motion stimulation
Eye motion
Stimulation
Eye motion
Power (a.u.)
Hz
Eye motion (vertical component)
Fixation
Vertical motion stimulation
Eye motion
Stimulation
Eye motion
Power (a.u.)
Hz

Figure S3

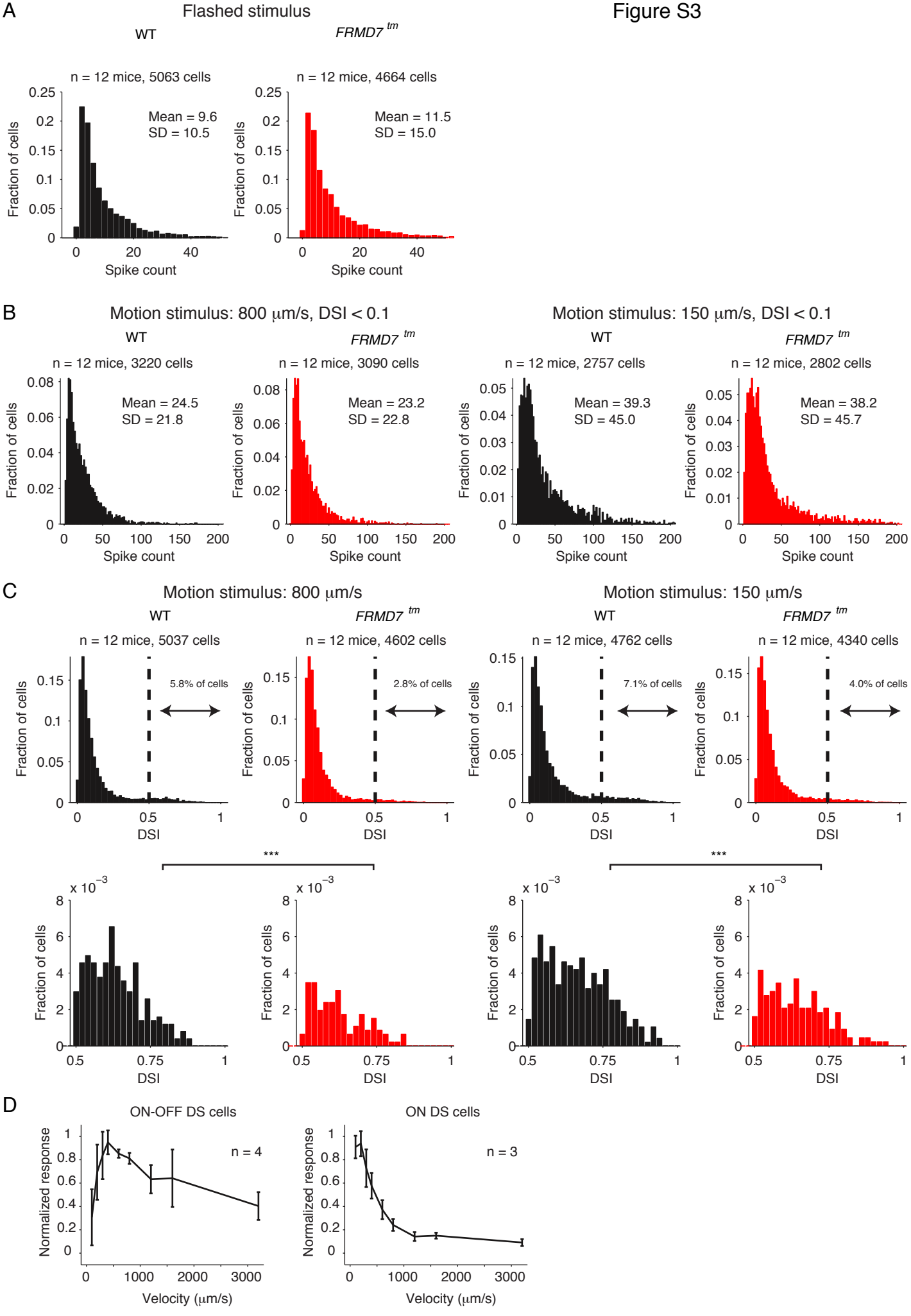
A
Flashed stimulus
WT
FRMD7 tm
n = 12 mice, 5063 cells
Mean = 9.6
SD = 10.5
n = 12 mice, 4664 cells
Mean = 11.5
SD = 15.0
Fraction of cells
Spike count
B
Motion stimulus: 800 μm/s, DSI < 0.1
Motion stimulus: 150 μm/s, DSI < 0.1
n = 12 mice, 3220 cells
Mean = 24.5
SD = 21.8
n = 12 mice, 3090 cells
Mean = 23.2
SD = 22.8
n = 12 mice, 2757 cells
Mean = 39.3
SD = 45.0
n = 12 mice, 2802 cells
Mean = 38.2
SD = 45.7
C
Motion stimulus: 800 μm/s
Motion stimulus: 150 μm/s
n = 12 mice, 5037 cells
5.8% of cells
n = 12 mice, 4602 cells
2.8% of cells
n = 12 mice, 4762 cells
7.1% of cells
n = 12 mice, 4340 cells
4.0% of cells
DSI
***
x 10−3
D
ON-OFF DS cells
n = 4
ON DS cells
n = 3
Normalized response
Velocity (μm/s)

Figure S4

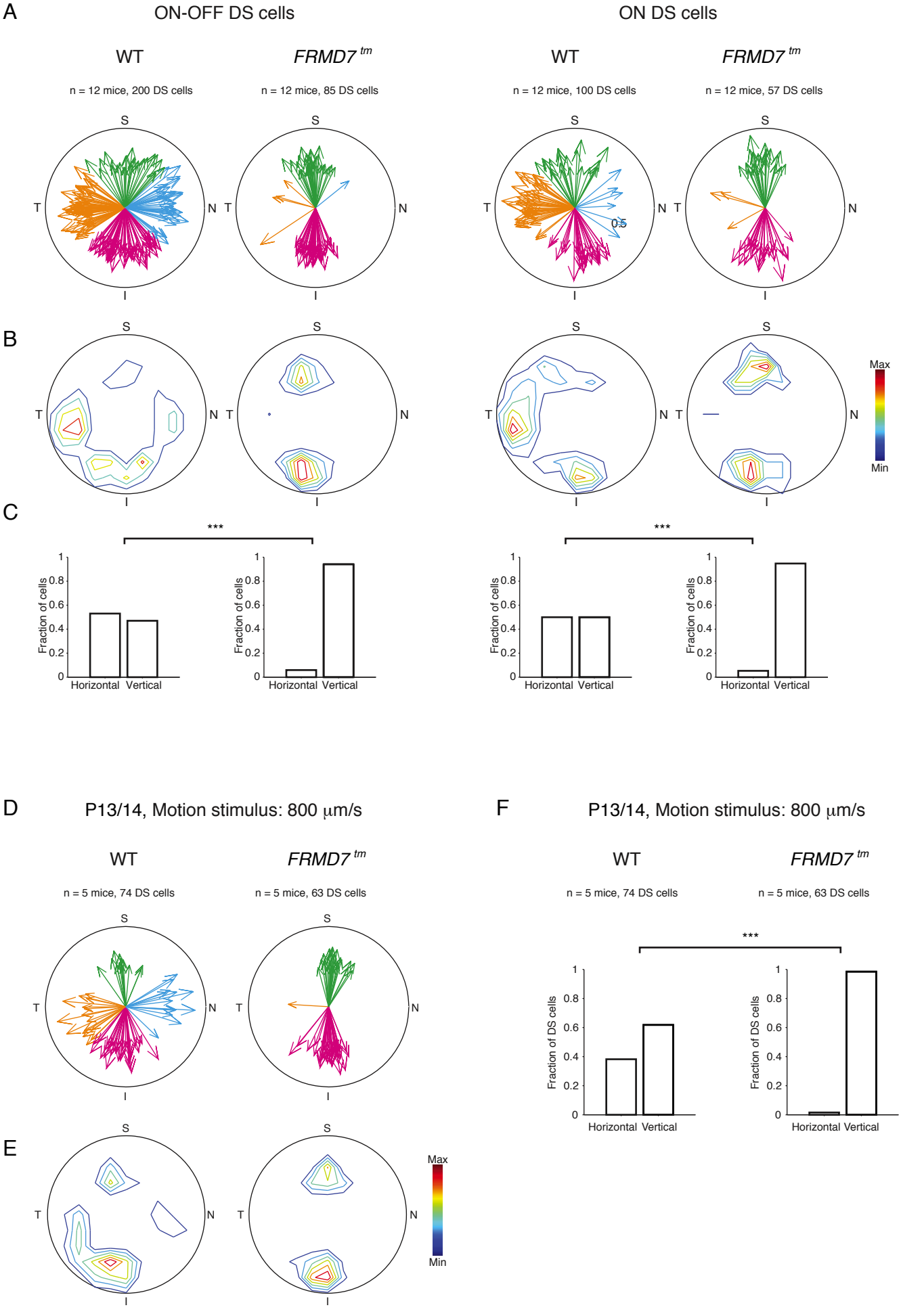
A
ON-OFF DS cells
ON DS cells
WT
FRMD7 tm
n = 12 mice, 200 DS cells
n = 12 mice, 85 DS cells
n = 12 mice, 100 DS cells
n = 12 mice, 57 DS cells
S
T
N
I
0.5
B
Max
Min
C
***
Fraction of cells
Horizontal
Vertical
D
P13/14, Motion stimulus: 800 μm/s
n = 5 mice, 74 DS cells
n = 5 mice, 63 DS cells
E
F
Fraction of DS cells

Figure S5

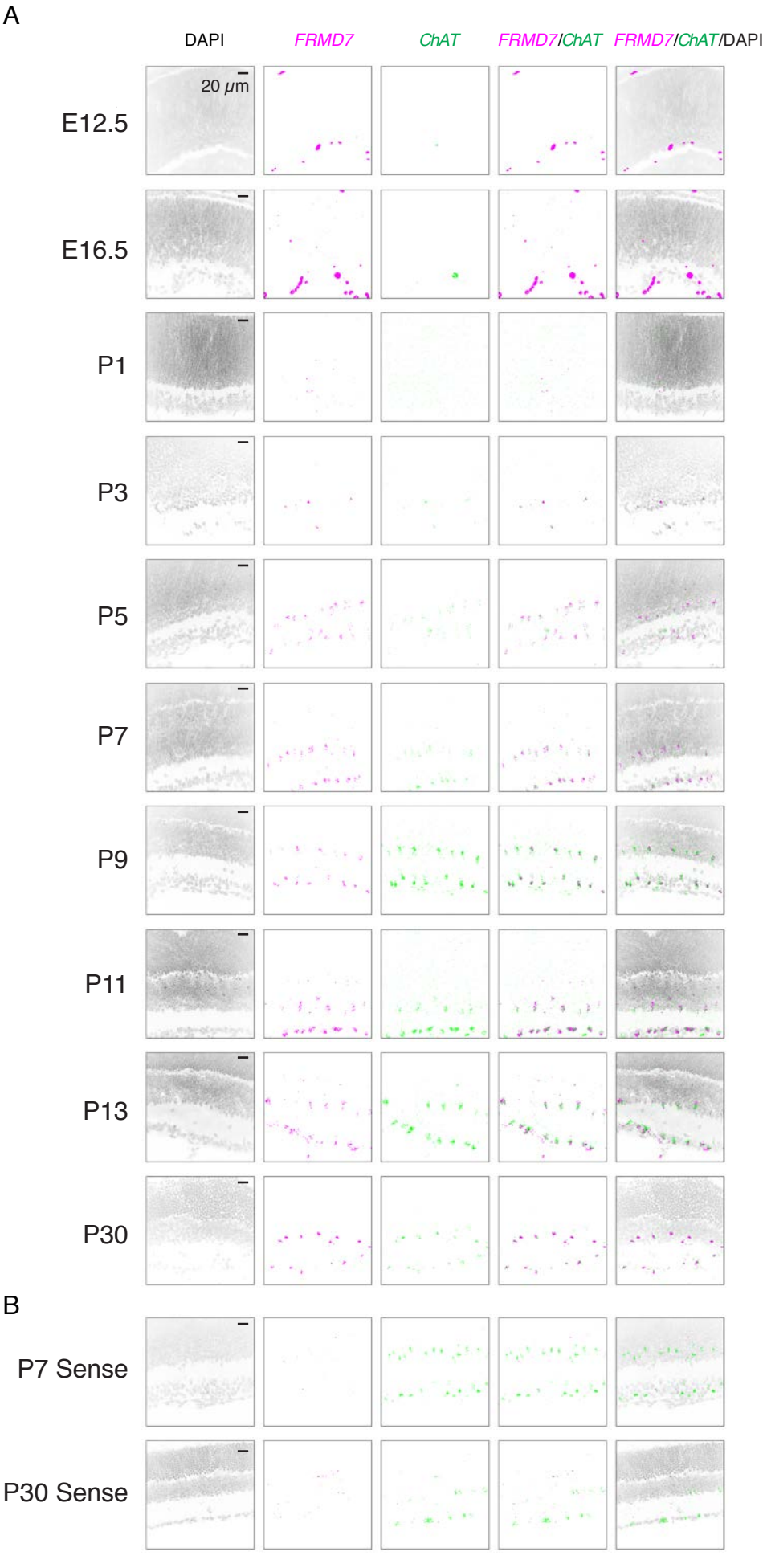
A
DAPI
FRMD7
ChAT
FRMD7/ChAT
FRMD7/ChAT/DAPI
20 μm
E12.5
E16.5
P1
P3
P5
P7
P9
P11
P13
P30
B
P7 Sense
P30 Sense

Figure S6

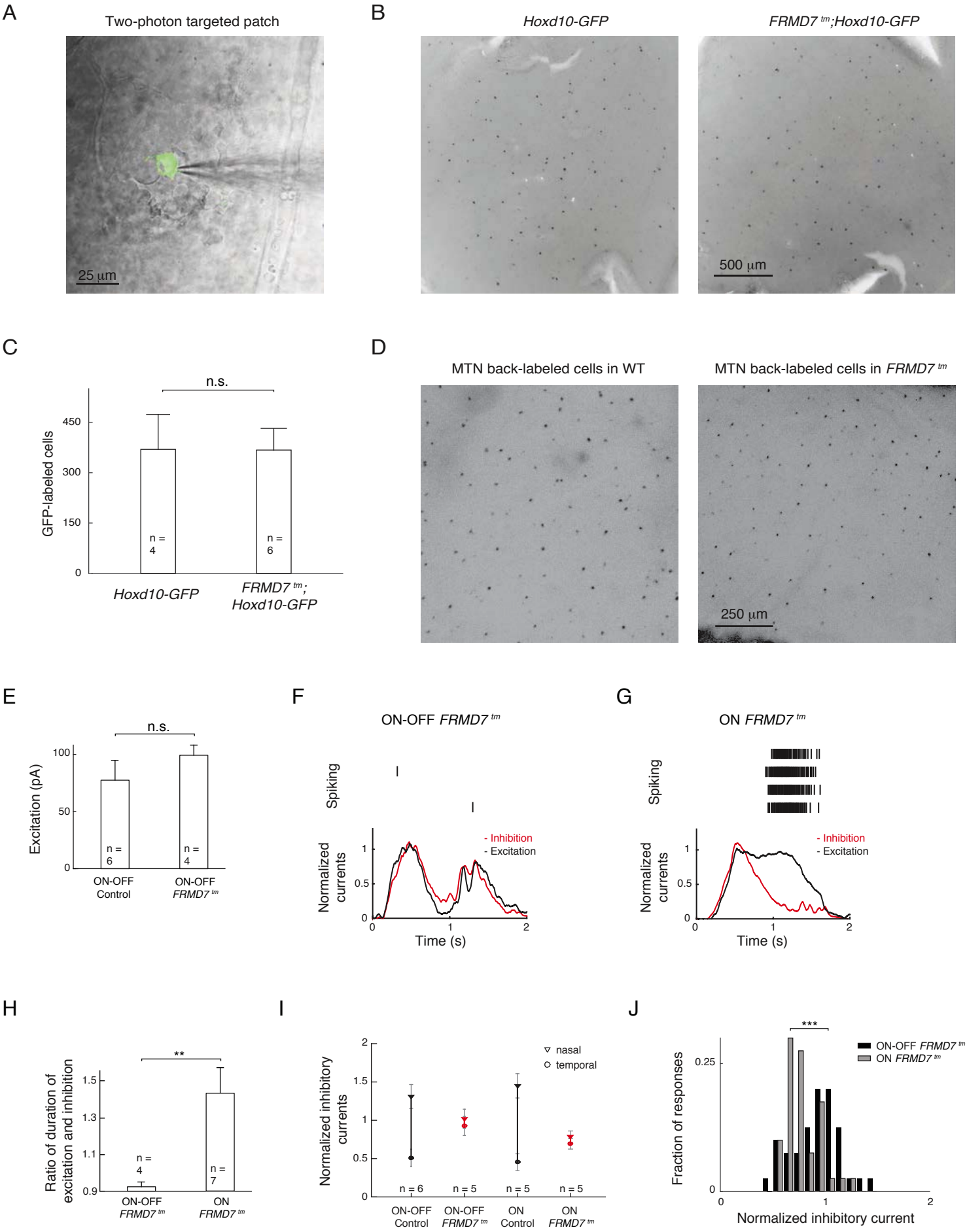
A
Two-photon targeted patch
25 μm
B
Hoxd10-GFP
FRMD7 tm;Hoxd10-GFP
500 μm
C
n.s.
GFP-labeled cells
450
300
150
0
n = 4
n = 6
Hoxd10-GFP
FRMD7 tm; Hoxd10-GFP
D
MTN back-labeled cells in WT
MTN back-labeled cells in FRMD7 tm
250 μm
E
n.s.
Excitation (pA)
100
50
0
n = 6
n = 4
ON-OFF Control
ON-OFF FRMD7 tm
F
ON-OFF FRMD7 tm
Spiking
Normalized currents
- Inhibition
- Excitation
Time (s)
G
ON FRMD7 tm
Spiking
Normalized currents
- Inhibition
- Excitation
Time (s)
H
**
Ratio of duration of excitation and inhibition
1.5
1.3
1.1
0.9
n = 4
n = 7
ON-OFF FRMD7 tm
ON FRMD7 tm
I
Normalized inhibitory currents
nasal
temporal
n = 6
n = 5
n = 5
n = 5
ON-OFF Control
ON-OFF FRMD7 tm
ON Control
ON FRMD7 tm
J
***
Fraction of responses
0.25
0
ON-OFF FRMD7 tm
ON FRMD7 tm
Normalized inhibitory current

Figure S7

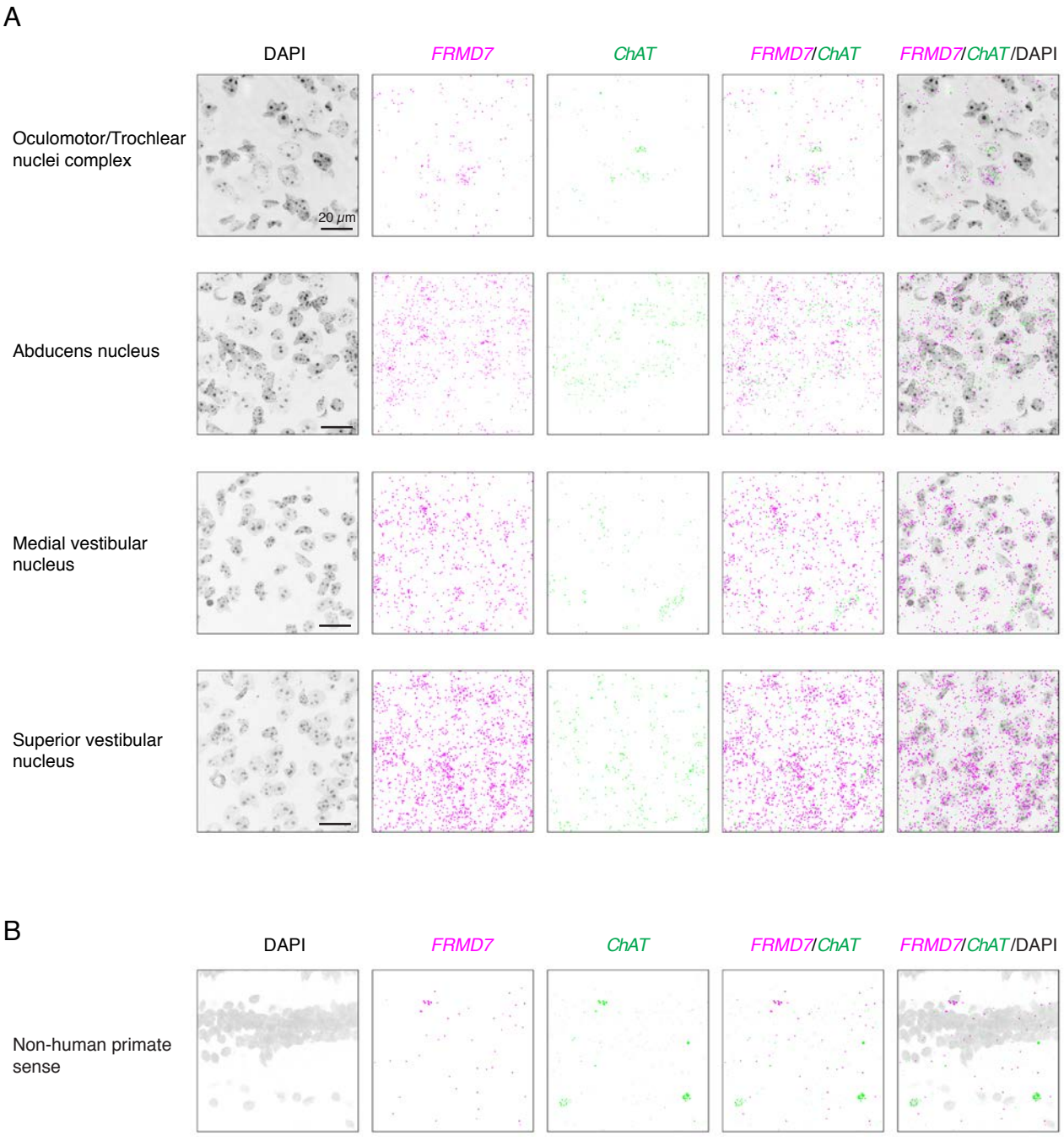
A
DAPI
FRMD7
ChAT
FRMD7/ChAT
FRMD7/ChAT/DAPI
Oculomotor/Trochlear nuclei complex
20 μm
Abducens nucleus
Medial vestibular nucleus
Superior vestibular nucleus
B
DAPI
FRMD7
ChAT
FRMD7/ChAT
FRMD7/ChAT/DAPI
Non-human primate sense

SUPPLEMENTAL FIGURE LEGENDS

Figure S1. Identification of *FRMD7* transcript variants in wild type and *FRMD7^{tm}* mice, related to Figures 1 and 3

(A) Schematic representation of predicted mRNAs in wild type (WT) and *FRMD7^{tm}* mice together with the primer locations (sequences corresponding to the names are shown in Experimental Procedures) and predicted RT-PCR products (P1-P7). Numbers (1-12) refer to the corresponding exon. The En2 fragment and iRES-LacZ are part of the cassette used to generate *FRMD7^{tm}* knock-in mice. (B) Agarose gel electrophoresis of the RT-PCR products of *FRMD7* mRNA in wild type (WT) and *FRMD7^{tm}* mice. Names of specific lanes correspond to predicted PCR products indicated in A. (C) Schematic representation of different *FRMD7* transcript variants cloned and sequenced from *FRMD7^{tm}* mice. Asterisks indicate frame-shift-generated stop codons. (D) RT-qPCR quantified expression levels of *FRMD7* transcript variants in *FRMD7^{tm}* mice. Individual transcripts were amplified using the oligonucleotide primers indicated in brackets. Expression level of the FRMD7-Mut-ex4-del transcript variant was determined by subtracting the level of FRMD7-WT (ex3F/ex4R primer pair amplified) transcript from the level of ex3F/ex5R primer pair amplified transcripts. (E) Comparison of the expression of FRMD7-WT transcript in wild type and *FRMD7^{tm}* mice using RT-qPCR. (F) LacZ is specifically expressed in starburst cells in the retina of *FRMD7^{tm}* mice. Confocal images of the GCL (top) and INL (bottom) of adult *FRMD7^{tm}* retina stained with antibodies for LacZ and ChAT. Black arrows indicate clustered LacZ signals.

Figure S2. Nystagmus and optokinetic reflex, related to Figure 1. (A) Eye movements produced by wild type (black) and *FRMD7^{tm}* (red) mice in response to motion in the superior direction on the retina. (B) Distribution of fixation points during fixation in a control human subject (left) and a subject with *FRMD7* mutation (right). (C) Quantification of data in B using the full-width-at-half-maximum values (FWHM) of fitted 2D Gaussian curves. (D) Power spectra (red traces, arbitrary units) of the horizontal (top) and vertical eye movements (bottom) of a human subject with *FRMD7* mutation during fixation (left) and during visual stimulation with gratings moving at 15 degrees/second (right). The panels demonstrating eye motion during motion stimulation also show the power spectrum of the visual stimulation (black traces). Note that the power spectra of stimulation and eye motion do not overlap when the human subject was stimulated with horizontal motion, but do overlap when stimulated with vertical motion.

Figure S3. Visual responses of retinal ganglion cells in wild type and *FRMD7^{tm}* mice, related to Figure 2. The figure shows data obtained with microelectrode arrays. Black is wild type, red is *FRMD7^{tm}*. (A) Distributions of the number of spikes in response to flashed stimuli in all recorded ganglion cells. (B) Distributions of peak responses to fast (left) and slow (right) motion stimulation in non-DS (DSI < 0.1) ganglion cells. (C) Upper panels, distribution of DSI in response

to fast (left) and slow (right) motion in all ganglion cells. Lower panels, same as shown in upper panels but only cells having a DSI of 0.5-1 are shown. (D) Velocity tuning of ON-OFF and ON cells. Number of spikes (normalized to the maximum) evoked by motion at different velocities in ON-OFF (left) and ON (right) cells. Error bars indicate SD.

Figure S4. Lack of horizontal direction selectivity in ON-OFF and ON cells in the retina of *FRMD7^{tm}* mice, related to Figure 2. The figure shows data obtained with microelectrode arrays. In A-C, the left two columns show ON-OFF DS cells and the right two columns ON DS cells (Experimental Procedures). The radius of each circle corresponds to DSI=1. (A) Polar plots showing the preferred directions (direction of an arrow) and direction selectivity index (DSI, length of an arrow) of individual DS cells (DSI > 0.5, each recorded DS cell is represented by an arrow) in wild type and *FRMD7^{tm}* retinas. The color code designates the different directions according to Figure 1A. (B) Contour plots showing the density of DS cells with different DSIs and preferred directions. Red indicates maximal density. (C) The proportion of horizontal (nasal and temporal) and vertical (superior and inferior) motion preferring DS cells in wild type and *FRMD7^{tm}* retinas. (D-F) Lack of horizontal direction selectivity in the retina of *FRMD7^{tm}* mice at P13/14. (D) Polar plots showing the preferred directions (direction of arrow) and direction selectivity index (DSI, length of arrow) of individual DS cells (DSI > 0.5, each recorded DS cell is represented by an arrow) in wild type and *FRMD7^{tm}* retinas. The color code designates the different directions according to Figure 1A. (E) Contour plots showing the density of DS cells with different DSIs and preferred directions. Red indicates maximal density. (F) The proportion of horizontal (nasal and temporal) and vertical (superior and inferior) motion preferring DS cells in wild type and *FRMD7^{tm}* retinas.

Figure S5. FRMD7 is specifically expressed in starburst cells in the mouse retina during development, related to Figure 3. (A) Confocal images of mouse retinal sections stained by double-label fluorescence *in situ* hybridization using antisense probes for mouse *FRMD7* mRNA and mouse *ChAT* mRNA as well as DAPI at different developmental stages. Large dots at E12.5 and E16.5 are non-specific signals. (B) Confocal images of mouse retinal section stained using sense probe for mouse *FRMD7* mRNA and antisense probe for mouse *ChAT* mRNA as well as DAPI at P7 and P30.

.

Figure S6. Characterization of genetically labeled DS cells in the retina of *FRMD7^{tm}* mice, related to Figures 4 and 5. (A) Overlay of infrared image (black-white) and two-photon microscope image (green) of the ganglion cell layer of *Hoxd10-GFP* mice during two-photon targeted patch-recording. GFP-labeled DS cell (green, center) is being recorded in cell-attached mode using a glass-pipette (dark shape on right side of green cell). (B) Epi-fluorescence microscope images of GFP-labeled cells (black) in fixed retinas after immunostaining in *Hoxd10*-GFP (left) and *FRMD7^{tm};Hoxd10-GFP* (right) mice. (C) Quantification of GFP-labeled cells counted in unstained, freshly dissected *Hoxd10*-GFP and

FRMD7^{tm};*Hoxd10-GFP* retinas. Data points represent mean ± SEM, n refers to the number of retinas. (D) Epi-fluorescence microscope images of MTN back-labeled cells (black) in wild type (left) and *FRMD7^{tm}* (right), unstained, dissected retinas. (E) Bar graph displaying amplitudes of excitatory input current to GFP-labeled ON-OFF cells in *Hoxd10*-GFP (Control) and *FRMD7^{tm}*;*Hoxd10-GFP* (*FRMD7^{tm}*) retinas. Data points represent mean ± SEM, n refers to the number of cells. (F, G) Spike raster plot (top, black, four repetitions) and normalized excitation (bottom, black) and inhibition (bottom, red) recorded in ON-OFF (F) and ON (G) example cells of *FRMD7^{tm}*;*Hoxd10-GFP* mice in response to motion. (H) Bar graph displaying the ratio of the duration of excitation and inhibition in ON-OFF cells and ON cells recorded in *FRMD7^{tm}*;*Hoxd10-GFP* mice. Data from the eight motion directions were averaged. Data points represent mean ± SEM, n refers to the number of cells. (I) Magnitudes of inhibitory currents evoked by stimulation with temporal (circles) or nasal (triangles) motion recorded in ON-OFF cells and (non-vertically tuned) ON cells in *Hoxd10*-GFP (Control, black) and *FRMD7^{tm}*;*Hoxd10-GFP* (*FRMD7^{tm}*, red) retinas. Values were normalized by the magnitude of inhibitory current evoked by a flashed-spot stimulus. Data points represent median values, temporal and nasal median values are connected with solid lines, ± SEM is shown by gray bars, n refers to the number of cells. (J) Histogram showing the distribution of inhibitory current magnitudes evoked by motion in eight directions recorded in ON-OFF cells (black, n=5) and (non-vertically tuned) ON cells (grey, n=5) in *FRMD7^{tm}*;*Hoxd10-GFP* retinas. Values were normalized by the magnitude of inhibitory current evoked by a flashed spot stimulus.

Figure S7. **FRMD7 is expressed in motor nuclei, which innervate extraocular muscles, and vestibular nuclei, related to Figures 6 and 8.** (A) Confocal images of oculomotor/trochlear nuclei complex (top), abducens nucleus (second row), medial vestibular nucleus (third row) and superior vestibular nucleus (bottom) of P11 wild type mouse brain sections stained by double-label fluorescence *in situ* hybridization using antisense probes for *FRMD7* mRNA and *ChAT* mRNA as well as DAPI. (B) Confocal images of non-human primate retinal section stained using sense probe for non-human primate *FRMD7* mRNA and antisense probe for non-human primate *ChAT* mRNA as well as DAPI.

Movie S1. Horizontal optokinetic reflex in head fixed wild type (left) and *FRMD7^{tm}* (right) mice, related to Figure 1. Stimulus is shown at the bottom.

EXTENDED EXPERIMENTAL PROCEDURES

Animals. Wild type mice (C57BL/6) were obtained from Charles River. *FRMD7^{tm}* mice refer to the homozygous female or hemizygous male *Frmd7$^{tm1a(KOMP)Wtsi}$* mice, which were obtained from the Knockout Mouse Project (KOMP)

Repository. A splicer acceptor-*IRES-lacZ* cassette is inserted into the intron between *FRMD7* exon 3 and exon 4, designed to result in the production of a truncated N-terminal part of the FRMD7 protein (68 amino acids) and LacZ. The integrity of the targeted genomic region in the *FRMD7*^{tm} mouse was confirmed by PCR by the International Mouse Phenotyping Consortium (IMPC). Genotyping of *FRMD7*^{tm} mice was carried out according to KOMP instructions. Both male and female *FRMD7*^{tm} mice were used in this study. The mRNA variants expressed from the mutant *FRMD7* locus in *FRMD7*^{tm} mice are described below in the section "Mouse FRMD7 mRNA analysis". *ChAT-Cre* mice (Ivanova et al., 2010) were obtained from Jackson Laboratory (strain: B6;129S6-*Chat*$^{tm1(cre)Lowl}$/J) and *Hoxd10-GFP* mice (Dhande et al., 2013) from Mutant Mouse Research and Resource Center (strain: STOCK Tg*(Hoxd10-EGFP)LT174Gsat/Mmucd*). Unless indicated otherwise, mice were between age P40 and P120. Mice were maintained in C57BL/6 background. A female cynomolgus monkey (Macaca fascicularis), was obtained from BioPRIM. Animals were housed in groups under maintained temperature (20-24°C), at least 40% humidity and a natural light cycle, and fed at least twice daily with a mixture of fruits and vegetables. Water and Kliba Nafag 3446 pellets (Kaiseraugst, Germany) were provided ad libitum. Euthanasia at age 19 was performed by intravenously applied 10 ml pentobarbital (Esconarkon, Streuli Pharma AG, Uznach, Switzerland). All animal procedures were performed in accordance with standard ethical guidelines (European Communities Guidelines on the Care and Use of Laboratory Animals, 86/609/EEC) and were approved by the Veterinary Department of the Canton of Basel-Stadt, Switzerland.

Human subjects. Eye movement was recorded from three male human subjects with congenital nystagmus (ages 19, 22 and 41) resulted from a hemizygous mutation in the FRMD7 gene as well as from four control subjects (ages 30, 30, 33, and 36). Human subjects with congenital nystagmus had a complete ophthalmologic examination, including slit-lamp examination, fundus examination and measurement of visual acuity. The mutations were c.685C>T (p.R229C) in exon 8 in the 19 and 22 year old subjects (from the same family) and c.673T>G (p.W225G) in exon 8 in the 41 year old subject. This prospective research was conducted in accordance with Good Clinical Practices. The research procedures followed the tenets of the Declaration of Helsinki, and all tests and examinations were performed after obtaining informed consent from all subjects. The study protocol was approved by the relevant Institutional Review Boards.

Eye movement detection. Eye tracking was performed using an ETL-200 eye tracking system (Iscan Inc., Woburn, Maine, USA). To visualize the pupil, eyes were illuminated with IR light and recorded with IR cameras, at 240 Hz in humans, and at 120 Hz in mice. The optokinetic reflex was quantified by counting the number of eye tracking movements (ETMs) as described previously (Cahill and Nathans, 2008). Briefly, the position of the pupil was plotted as a function of time, the derivative of this signal was calculated and a threshold was set. Events above threshold were counted as ETMs.

The threshold was adjusted in wild type mice and in control human subjects so that all visually assessed ETMs were detected. This threshold was then applied to data from *FRMD7*^{tm} mice and human subjects with *FRMD7* mutation.

Visual stimulation, controlled by software written in Python (python.org), or PsychoPy (psychopy.org), was presented on a computer monitor. For humans, the monitor was placed 65 cm from the eye, which corresponded to 44° of visual angle horizontally and 28° vertically. The head was kept in place with a chin rest. For eye fixation, a spot of 0.25° diameter was presented for 15 s in the center of the monitor. For motion stimulation, black and white gratings (0.5 duty cycle) with 6° wide bars were moved at 15°/s. One degree corresponds to 300 µm retinal distance in humans (Oyster, 2006). For mice, visual stimulation was executed as described previously (Yonehara et al., 2009), except that here two monitors were placed in a 'V' position in front of the mouse for binocular stimulation. The head of the mouse was fixed with a head holder, and the body was restrained in a foam jacket. For motion stimulation black and white gratings (0.5 duty cycle) with 20°-wide bars were moved at 10°/s. One degree corresponds to 31 µm retinal distance in mice (Remtulla and Hallett, 1985).

AAV production. To obtain the production plasmid for serotype-7 AAV-EF1a-DIO-TVA66T-WPRE-hGHpA, we linearized pAAV-EF1a-double floxed-hChR2(H134R)-EYFP-WPRE-hGHpA (kindly provided by K. Deisseroth, Stanford University) using NheI/AscI sites. A TVA66T insert with NheI/AscI overhand sites was synthesized (GenScript) based on the CAG-Flex-TC66T sequence, which was obtained from Addgene (plasmid # 48331) and cut using NheI/AscI. pAAV-hSyn1(S)-FLEX-tdTomato-T2A-SypEGFP-WPRE was obtained from Addgene (plasmid # 51509). AAV was made according to standard protocols. Genome copy (GC) number titration was performed using real-time PCR (Applied Biosystems, TaqMan reagents).

Rabies virus production. G-coated SADΔG-GFP rabies virus (Wickersham et al., 2007a)(provided by K.K. Conzelmann, Munich) was amplified by infecting B7GG cells. EnvA-coated SADΔG-GFP rabies virus was obtained by infecting BHK-EnvARGCD cells with the G-coated viruses (Wickersham et al., 2007b). Viruses were concentrated by ultracentrifugation as described before (Ghanem et al., 2012). Titration using plaque-forming units (pfu) was performed by infecting BHK cells and HEK293T-TVA800 cells with G-coated virus and EnvA-coated virus, respectively.

Virus injections. Mice were anesthetized with an intraperitoneal injection of ketamine (108 mg/kg) and xylazine (14.4 mg/kg). To label starburst cells with GFP, serotype-7 AAV-EF1a-DIO-TVA66T-WPRE-hGHpA in PBS (1.8×10^{15} GC/ml) was loaded into pulled-glass pipettes (tip inner diameter 20-30 µm) and 2 µl was injected intravitreously into the

eye of *ChAT-Cre* and *FRMD7^{tm}*;*ChAT-Cre* mice using a pneumatic microinjector (Narishige, IM-11-2). Two weeks later, EnvA-coated SADΔG-GFP rabies virus (10^{10} pfu/ml) was loaded into pulled-glass pipettes and 2 μl was injected intravitreously into the eye. One week later the retinas were isolated and fixed with 4% paraformaldehyde. To label starburst cells with synaptophysin-GFP, serotype-8 AAV-hSyn1(S)-FLEX-tdTomato-T2A-SypEGFP-WPRE-hGHpA (3.72×10^{11} GC/ml) was loaded into a Hamilton syringe and 2 μl was injected intravitreously into the eye of *ChAT-Cre* and *FRMD7^{tm}*;*ChAT-Cre* mice. Three weeks later the retinas were isolated and fixed with 4% paraformaldehyde.

Fluorescent *in situ* hybridization. Double-label fluorescent *in situ* hybridization on retinal sections from mice and non-human primate, and brain sections from mice was carried out using the RNAscope Multiplex Fluorescent Assay (Advanced Cell Diagnostics) according to the manufacturer's instructions. Briefly, dissected retinas were fixed with 4% paraformaldehyde, cryoprotected with 30% sucrose in PBS, embedded in OCT compound, frozen on dry ice, and cryosectioned at 20 μm. To prepare embryonic retinal sections, embryos were fixed overnight in 4% paraformaldehyde in PBS and washed with PBS for at least 1 day at 4°C, cryoprotected with 30% sucrose in PBS, embedded in OCT compound, frozen on dry ice, and cryosectioned at 20 μm. To prepare brain sections, animals were transcardially perfused with 4% paraformaldehyde and the brains were post-fixed in 4% paraformaldehyde overnight at 4°C, cryoprotected with 30% sucrose in PBS, embedded in OCT compound, frozen on dry ice, and cryosectioned at 30 μm. Mouse retinal or brain sections were hybridized with antisense and sense probes for mouse *FRMD7* mRNA (Genbank: NM_001190332.1) and antisense probe for mouse *ChAT* mRNA (Genbank: NM_009891.2), and signals were amplified. Non-human primate retinal sections were hybridized with antisense and sense probes for macaca fasicularis *FRMD7* mRNA (Genbank: XM_005594586.1) and antisense probe for macaca fasicularis *ChAT* mRNA (Genbank: XM_005565136.1), and signals were amplified. Slides were stained with DAPI and mounted with Prolong Gold (Life Technologies). Positive staining was identified as punctate dots present within the cells.

Retrograde and anterograde tracer injections. To label ON DS cells projecting to the MTN, adult mice were anesthetized with an intraperitoneal injection of ketamine/xylazine and head-fixed with a stereotaxic instrument (Narishige, SR-5M). Cholera toxin subunit B Alexa Fluor 488 conjugate (Invitrogen, C34775) at 1 mg/μl in PBS was loaded into pulled-glass pipettes (tip inner diameter 20-30 μm), and 100 μl was injected into the MTN using a pneumatic microinjector (Narishige, IM-11-2).

To label retinal ganglion axons innervating retino-recipient nuclei, mice were anesthetized with an intraperitoneal injection of ketamine/xylazine. Cholera toxin subunit B Alexa Fluor 594 conjugate (Invitrogen, C34777) or 647

conjugate (C34778) at 1 mg/µl in PBS was loaded into pulled-glass pipettes (tip inner diameter 20-30 µm) and 2 µl was injected intravitreously into the eye. One week later brains were isolated and used for immunohistochemistry.

Preparation of retina for electrophysiology. Light-adapted mice were used for recordings. Retinas were isolated under dim red light (FGL610, Thorlabs) in Ringer's medium (in mM: 110 NaCl, 2.5 KCl, 1 $CaCl_2$, 1.6 $MgCl_2$, 10 d-glucose, 22 $NaHCO_3$) bubbled with 5% CO_2, 95% O_2. The dorsal side of the retina was marked with a small incision, which was later used to align the visual stimulation to the retinal axes. For microelectrode array recordings, a retinal patch was placed ganglion-cell-side-down on the microelectrode array. To secure the retina on the microelectrode array, a permeable membrane (polyester, 10 µm thickness, 0.4 µm pore size) was lightly pressed against the tissue. For patch-clamp recordings, the retina was mounted ganglion-cell-layer-up on a filter paper (Millipore) with a 2×2 mm aperture to allow for visual stimulation of the photoreceptors. During microelectrode array and patch-clamp recordings, the retina was kept at 35°C and was continuously superfused with Ringer's medium bubbled with 5% CO_2, 95% O_2.

Microelectrode array recordings. Recordings and light stimulation were performed as described before (Fiscella et al., 2012). In most experiments, CMOS-based microelectrode arrays with 11,011 platinum electrodes with diameters of 7 µm and electrode center-to-center distances of 18 µm over an area of 2×1.75 mm^2 were used (Fiscella et al., 2012; Frey et al., 2009, 2010). In some experiments CMOS-based microelectrode arrays with 26,400 platinum electrodes over an area of 3.85×2.1 mm^2 and 1,024 readout channels and a center-to-center electrode distance of 17.5 µm were used (Ballini et al., 2014; Müller et al., 2015) .

Visual stimuli. Flashed stimulus: this stimulus was used to determine if a cell was ON-OFF (responding to both light increments and decrements) or ON (responding to light increments only). A positive-contrast square stimulus (0.2×0.2 mm^2) was turned on for one second and turned off for one second in 5 repetitions. The stimulus moved sequentially in discrete non-overlapping steps over an area of ~1 mm^2 with a background irradiance of 0.2 µW/cm^2 and a square stimulus irradiance of 47 µW/cm^2. Motion stimulus: this stimulus was used to test direction selectivity. A 1 mm wide and 0.5 mm long (perpendicular to stimulus motion) white bar (background irradiance 0.2 µW/cm^2 and stimulus irradiance 47 µW/cm^2) moved across the retina at a velocity of 0.15 or 0.8 mm/s, along eight equidistant angular directions radially spaced at 45°. The large bar width (1 mm) was chosen to separate ON and OFF responses. Each motion stimulus was repeated five times.

Spike sorting and data analysis. For spike sorting we used a fully automatic two-stage procedure that first identified spike templates for each neuron (Marre et al., 2012; Prentice et al., 2011) and then classified each spike using template matching (Franke et al., 2015). Spike data obtained from stimulus repetitions were averaged. The direction selectivity index (DSI) and preferred direction of a neuron were defined as described previously (Taylor and Vaney 2002). Briefly, eight vectors were formed, each associated with motion along a direction. The length of each vector was the mean number of spikes across stimulus repetitions along the relevant direction and the angle of the vector was the angle corresponding to the motion direction (0°, 45°, 90°, 135°, 180°, 225°, 270°, 315°). The DSI and preferred direction of the neuron were defined as the length and angle of the sum of the eight vectors divided by the sum of the lengths of the eight vectors (normalized vector sum), respectively. The horizontal and vertical DSIs were defined as the length of the horizontal and vertical components of the normalized vector sum. In the analysis of microelectrode electrode array data, we defined a neuron as direction selective if its DSI was higher than 0.5.

Slow- and fast-motion preferring DS cells were segregated using a velocity index (VI).

$$VI = (rF - rS)/(rS + rF)$$

rF is the maximum response of a cell across the eight stimulus directions using a motion velocity of 0.8 mm/s, and rS is the maximum response of the same cell across the eight stimulus directions using a motion velocity of 0.15 mm/s. VI ranges from −1 to 1. Cells with $VI > -0.5$ were categorized as fast DS cells and with $VI \leq -0.5$ as slow DS cells.

ON-OFF and ON DS cells were segregated using an ON-OFF index (OOI).

$$OOI = (rON - rOFF)/(rON + rOFF)$$

rON is the maximum response of a cell to a positive contrast, flashed stimulus stepped across its receptive field, and rOFF is the maximum response of a cell to a negative contrast, flashed stimulus stepped across its receptive field. The OOI ranges from −1 to 1. Cells with $|OOI| < 0.8$ were categorized as ON-OFF cells and cells with $OOI > 0.8$ as ON cells.

Two-photon targeted patch clamp recording. *Hoxd10-GFP* and *FRMD7^{tm}*;*Hoxd10-GFP* mice were used for targeted recordings. Cells back-labeled from the MTN with cholera toxin subunit B Alexa Fluor 488 conjugate were targeted to record from vertically tuned ON DS cells in wild type and *FRMD7^{tm}* mice. The two-photon microscope system for targeted patch clamp recordings from GFP- or Alexa488-labeled cells, including the light pathways for visual stimulation of the retina, has been described before (Farrow et al., 2013). GFP- or Alexa488-labeled cells were targeted using a two-photon microscope equipped with a Mai Tai HP two-photon laser (Spectra Physics), set to 920 nm, which was integrated into the electrophysiological setup. The two-photon fluorescence image was overlaid on an IR image acquired with a

CCD camera (SPOT Visitron Systems). The infrared light was produced with a digital light projector (V300X, NEC) and a 750 ± 25 nm filter. Spike recordings and whole-cell recordings were performed with borosilicate glass electrodes (BF100-50-10, Sutter Instruments), pulled to 5-7 MΩ, using an Axon Multiclamp 700B amplifier. Signals were digitized at 10 kHz and acquired using software written in LabVIEW (National Instruments). Spike recordings were made in loose cell-attached mode and electrodes were filled with Ringer's solution. Whole-cell recordings were made in voltage-clamp mode and electrodes were filled with (in mM) 112.5 $CsCH_3SO_3$, 1 $MgSO_4$, 7.8×10^{-3} $CaCl_2$, 0.5 BAPTA, 10 HEPES, 4 ATP-Na_2, 0.5 GTP-Na_3, 5 lidocaine N-ethylbromide (Qx314-Br) and 7.75 neurobiotin chloride; pH adjusted to 7.2. Inhibitory and excitatory currents ('inhibition' and 'excitation') were separated by voltage clamping the cell to the equilibrium potential of unselective cation channels (0 mV) or the equilibrium potential of chloride (−60 mV), respectively (Roska and Werblin, 2001). The light for retinal stimulation was generated by a digital light projector (V300X, NEC) at a refresh rate of 75 Hz, and focused on the retinal photoreceptor layer after passing a neutral density filter (ND40). After targeting, the recorded cell was kept at a constant grey background level with a light intensity of 60 $\mu W/cm^2$ on which the positive or negative contrast stimulus was displayed. The moving stimulus consisted of a 300 µm-diameter light spot with positive 50% contrast (122 $\mu W/cm^2$), which moved across the retina in eight directions at 300 µm/s. The flashed stimulus consisted of a 300 µm-diameter light spot with positive or negative 50% contrast centered to the soma of the cell. All stimuli were repeated five times. The visual stimulation was controlled via custom-made software written in Python (Python Software Foundation).

Data were analyzed offline using MATLAB (Mathworks). Spikes were detected by thresholding. Spike data and inhibitory currents were averaged across stimulus repetitions. Responses were quantified by counting the spike events for the cell-attached data and measuring the amplitude of the inhibitory current for the whole-cell data for each motion direction. From these responses the DSI and the horizontal DSI were computed for both spike tuning and inhibitory tuning, as described in the microelectrode array section. Polar plots of the spike tuning and quantification of spiking DSI were only made for cells responding with at least 15 spikes in four stimulation trials. Spike rates were obtained by convolving the spike train with a Gaussian window (sigma = 35 ms). Inhibitory current traces were smoothed using the MATLAB smooth function with a span of 0.3 s for plotting the example cells (Figures 4-5) or a span of 0.01 s for plotting the time course of inhibition and excitation (Figures S6F-S6G). The duration of excitatory and inhibitory currents was defined by the time, during which the current was higher than 75% of its maximal value. For normalization of motion-evoked magnitudes of inhibitory currents, values were divided by the magnitude of the inhibitory current evoked by the flashed spot stimulus for each cell.

Mouse *FRMD7* mRNA analysis. Total RNA was extracted from wild type and *FRMD7^{tm}* retinas using Trizol reagent (Invitrogen). To form cDNA, RNA was reverse transcribed using random hexamers and the Superscript III thermostable RT system (Invitrogen) according to the manufacturer's instructions. *FRMD7* splice variants were determined from wild type and *FRMD7^{tm}* cDNA by PCR amplification using the following primers: ex2F (5'-cgctcttcaacctgagctg), ex3R (5'-cttgcttcgttatgggcttc), ex3F (5'- tggaacttctgaagcccataa), ex4R (5'-agttcttcccgaagatgtcc), ex5R (5'-atgtgcgacaccattaaagc), En2R (5'-aactcagccttgagcctctg), lacZR1 (5'-caccacgctcatcgataattt), lacZF1 (5'-ttcaacatcagccgctacag), and lacZR2 (5'-tttcaggttcaggggaggtgtg) (Figure S1A). PCR products were identified on agarose gel (Figure S1B), extracted, cloned using the TOPO Cloning Kit (Invitrogen) and sequenced, and the sequences were analyzed (Figures S1C-S1E). In wild type mice we identified a single transcript variant across exon 2 to exon 5 (FRMD7-WT, see below). In *FRMD7^{tm}* mice we found three major transcript variants (FRMD7-Mut, FRMD7-Mut-ex4-del and FRMD7-WT). FRMD7-Mut-ex4-del had two minor variants (FRMD7-Mut-ex4-del-v1 and FRMD7-Mut-ex4-del-v2). The FRMD7-Mut transcript contains the first three exons of *FRMD7* mRNA and the non-genomic *En2-IRES-LacZ* cassette. In FRMD7-Mut-ex4-del-transcripts exon 4 is deleted. Due to inserted, in-frame stop codons, both FRMD7-Mut and FRMD7-Mut-ex4-del transcripts are predicted to produce a truncated protein consisting of exons 1 to 3 in which the FERM-N domain of *FRMD7* is disrupted and FERM-M and FERM-C domains omitted. The presence of (low levels of) wild type transcript is likely due to alternative splicing that skips the inserted *LacZ* cassette. The 5-prime region of the *FRMD7* transcript variants (Figure S1C) are shown below, the first in-frame stop codon is shown underlined and bold, the primer pair used to amplify the transcript fragment is shown in brackets.

FRMD7-Mut (ex3F/lacZR1):

tggaacttctgaagcccataacgaagcaagtcaaaaatcccaggtcccgaaaaccaaagaagaagaaccctaacaaagaggacaagcggcctcgcacagccttcactgctga
gcagctccagaggctcaaggctgagtttcagaccaacaggtacctgacagagcagcggcgccagagtctggcacaggagctcggtacccggaagatctggactctagagaa
ttccgcccctctccctccccccccccctaacgttactggccgaagccgcttggaataaggccggtgtgcgtttgtctatatgttatttttccaccatattgccgtcttttggcaatg**tga**gg
gcccggaaacctggccctgtcttcttgacgagcattcctaggggtctttcccctctcgccaaaggaatgcaaggtctgttgaatgtcgtgaaggaagcagttcctctggaagcttctt
gaagacaaacaacgtctgtagcgacccttttgcaggcagcggaacccccccacctggcgacaggtgcctctgcggccaaaagccacgtgtataagatacacctgcaaaggcgg
cacaaccccagtgccacgttgtgagttggatagttgtggaaagagtcaaatggctctcctcaagcgtattcaacaaggggctgaaggatgcccagaaggtaccccattgtatggg
atctgatctggggcctcggtgcacatgctttacatgtgtttagtcgaggttaaaaaacgtctaggcccccccgaaccacggggacgtggttttcctttgaaaaacacgatgataagctt
gccacaaccatggaagatcccgtcgttttacaacgtcgtgactgggaaaaccctggcgttacccaacttaatcgccttgcagcacatccccctttcgccagctggcgtaatagcga
agaggcccgcaccgatcgcccttcccaacagttgcgcagcctgaatggcgaatggcgctttgcctggtttccggcaccagaagcggtgccggaaagctggctggagtgcgat
cttcctgaggccgatactgtcgtcgtcccctcaaactggcagatgcacggttacgatgcgcccatctacaccaacgtgacctatcccattacggtcaatccgccgtttgttcccacg
gagaatccgacgggttgttactcgctcacatttaatgttgatgaaagctggctacaggaaggccagacgcgaattatttttgatggcgttaactcggcgtttcatctgtggtgcaacg

ggcgctgggtcggttacggccaggacagtcgtttgccgtctgaatttgacctgagcgcatttttacgcgccggagaaaaccgcctcgcggtgatggtgctgcgctggagtgacg
gcagttatctggaagatcaggatatgtggcggatgagcggcattttccgtgacgtctcgttgctgcataaaccgactacacaaatcagcgatttccatgttgccactcgctttaatgat
gatttcagccgcgctgtactggaggctgaagttcagatgtgcggcgagttgcgtgactacctacgggtaacagtttctttatggcagggtgaaacgcaggtcgccagcggcacc
gcgcctttcggcggtgaaattatcgatgagcgtggtg

FRMD7-Mut-ex4-del-v1(ex3F/ex5R):

tggaacttctgaagcccataacgaagcaagtcaaaaaggtatctttttactcttcaaataaagaaggatttggctctgggaaggcttccatgcag**tga**caactgcacagctttaatgg
tgtcgcacat

FRMD7-Mut-ex4-del-v2 (ex3F/ex5R):

tggaacttctgaagcccataacgaagcaagtcaaaaatccaggtatctttttactcttcaaa**taa**agaaggatttggctctgggaaggcttccatgcagtgacaactgcacagcttta
atggtgtcgcacat

FRMD7-WT (ex3F/ex5R):

tggaacttctgaagcccataacgaagcaagtcaaaaatcctaaggaggttgttttcaaatttatggtgaaatttttcccagtggaccccggacatcttcgggaagaactcacaaggt
atctttttactcttcaaataaagaaggatttggctctgggaaggcttccatgcagtgacaactgcacagctttaatggtgtcgcacat

In RT-qPCR analysis the level of the three major transcript variants were determined relative to 18S rRNA (Figures S1D-S1E). The phenotype observed in *FRMD7*^{tm} mice likely results from the significant decrease in the level of the FRMD7 protein. If, however, the truncated proteins made from the mutant transcripts are not degraded, it is possible that they act as dominant negative regulators of FRMD7 function.

Immunohistochemistry. Mouse retinas were fixed for 30 min in 4% (wt/vol) paraformaldehyde in PBS (in mM: 137 NaCl, 2.7 KCl, 4.3 Na_2HPO_4, 1.47 KH_2PO_4; pH 7.4) and washed with PBS for at least 1 day at 4°C. Non-human primate retinas were fixed for one or two days in 4% paraformaldehyde in PBS and washed with PBS for at least 1 day at 4°C. To stain the mouse brains, animals were transcardially perfused with 4% paraformaldehyde. The brains were post-fixed in 4% paraformaldehyde overnight at 4°C and sectioned at 150 µm using a vibratome (Leica, VT1000S). To aid penetration of the antibodies, retinas were frozen and thawed three times after cryoprotection with 30% (wt/vol) sucrose in PBS. For staining with anti-β galactosidase, antigen retrieval was carried out by incubating retinas in Tris-EDTA buffer (10 mM Tris, 1 mM EDTA, 0.05% Tween20, pH 8.0) for 30 min at 80°C. All other procedures were carried out at room temperature, except for the secondary antibody reaction. After washing in PBS, retinas were blocked for 1 h in 10%

(vol/vol) normal donkey serum (NDS; Chemicon), 1% (wt/vol) bovine serum albumin (BSA), and 0.5% (vol/vol) TritonX-100 in PBS. Primary antibodies were incubated for 6-7 days in 3% (vol/vol) NDS, 1% (wt/vol) BSA, 0.02% (wt/vol) sodium azide, and 0.5% (vol/vol) TritonX-100 in PBS. Secondary antibodies were incubated for one day at 4°C in 3% (vol/vol) NDS, 1% (wt/vol) BSA, and 0.5% (vol/vol) TritonX-100 in PBS together with streptavidin-Alexa Fluor 633 (Invitrogen, 1:200) and DAPI (4',6-diamidine-2-phenylindole dihydrochloride, Roche Diagnostics, 10 µg/ml) in some experiments. DAPI binds to DNA and, therefore, labels nuclei. After a final wash in PBS, retinas were embedded in Prolong Gold antifade (Life Technologies).

The following sets of primary and secondary antibody combinations were used for staining retinas:
(i) Primary: rabbit anti-FRMD7 (1:100). This affinity-purified polyclonal antibody was raised against the 16 amino acid C-terminal peptides of FRMD7 (Ac – SFATPGAEDRTLLKPC – NH2; Eurogentech). Secondary: donkey anti-rabbit IgG conjugated with Alexa Fluor 488 or 568 (1:200, Invitrogen). (ii) Primary: goat anti-ChAT (1:200, AB144P, Chemicon). Secondary: donkey anti-goat IgG conjugated with Alexa Fluor 488 or 568 (1:200, Invitrogen). (iii) Primary: rabbit anti-GFP (1:200, A11122, Invitrogen). Secondary: donkey anti-rabbit IgG conjugated with Alexa Fluor 488 (1:200, Invitrogen). (iv) Primary: rat anti-GFP (1:500, 04404-84, Nacalai). Secondary: donkey anti-rat IgG conjugated with Alexa Fluor 488 (1:200, Invitrogen). (v) Primary: chicken anti-β galactosidase (1:200, AB9361, abcam). Secondary: donkey anti-chicken IgY conjugated with Alexa Fluor 488 (1:200, Jackson ImmunoResearch).

Confocal analysis. Fluorescent *in situ* hybridization and immunohistochemistry signals in the retinas and brain sections were analyzed using a Zeiss LSM 700 confocal microscope. *In situ* hybridization signals were assessed from 1024×1024 pixel z-stack images at 0.35 µm z steps taken with a 63× oil immersion lens, numerical aperture (NA) 1.3. Immunohistrochemistry signals were assessed from 1024×1024 pixel z-stack images at 0.35 µm z steps taken with a 63× oil immersion lens, NA 1.3 or a 40× oil immersion lens, NA 1.0. Images were processed using Imaris (Bitplane), Fiji, or Mathematica (Wolfram). For quantification of fluorescent *in situ* hybridization, at each developmental time point (E12.5, E16.5, P1, P3, P5, P7, P9, P11, P13, and P30) we counted the number of punctuated dots for *ChAT* and *FRMD7* mRNAs present within the cell for five cells semi-automatically using the Imaris Spot function. To quantify the number of starburst cells in wild-type and *FRMD7*^{tm} retina, the ChAT-positive cells were counted manually from confocal images of anti-ChAT-stained retinas in Fiji. To quantify GFP-labeled starburst cell processes, we first drew a convex polygon by connecting the outer tips of the processes, and defined the area of the polygon as the dendritic field size in Fiji. For the dendritic asymmetry index, we determined the ratio between the widest and narrowest diameters of the polygon and expressed this as a percentage. The number of primary processes was counted in 3D-reconstructed confocal images in

Imaris. To quantify the co-stratification of neurobiotin-filled DS cell dendrites and anti-ChAT-labeled starburst cell processes in retinas of *Hoxd10-GFP* and *FRMD7^{tm}*;*Hoxd10-GFP* mice, we first determined the fluorescence intensity profile for neurobiotin and ChAT signals along the depth of the retina on the side view of the confocal z-stack in Fiji. Next, Full Width at Half Maximum for neurobiotin and ChAT signals were determined and their overlap at each of the proximal and distal strata within the inner plexiform layer was determined. To quantify GFP-labeled cells in the retinas of *Hoxd10-GFP* and *FRMD7^{tm}*;*Hoxd10-GFP* mice, the GFP-expressing cells were counted manually from epi-fluorescence stereomicroscopic (Olympus SZX16) images of non-stained, freshly dissected retinas.

Statistical Analysis. We used the following statistical tests. Mann-Whitney-Wilcoxon test: Figures 1C-1E, 1H-1J, 3C, 3E, 3H, 4E-4F, 5B, 5D, S1E, S2C, S6C, S6E, and S6H. Chi-square or Fisher exact test (if 'n' in a category ≤ 5): Figures 2C, S4C, and S4F. Hodges-Ajne test: Figure 7C. Kolmogorov-Smirnov test: Figures 2F, S3C and S6J. Statistical significance is noted by * for $p < 0.05$, ** for $p < 0.01$, and *** for $p < 0.001$. Not significant is denoted as n.s. for $p \geq 0.05$.

SUPPLEMENTAL REFERENCES

Ballini, M., Muller, J., Livi, P., Yihui Chen, Frey, U., Stettler, A., Shadmani, A., Viswam, V., Lloyd Jones, I., Jackel, D., et al. (2014). A 1024-Channel CMOS Microelectrode Array With 26,400 Electrodes for Recording and Stimulation of Electrogenic Cells In Vitro. IEEE J. Solid-State Circuits *49*, 2705–2719.

Cahill, H., and Nathans, J. (2008). The optokinetic reflex as a tool for quantitative analyses of nervous system function in mice: application to genetic and drug-induced variation. PloS One *3*, e2055.

Farrow, K., Teixeira, M., Szikra, T., Viney, T.J., Balint, K., Yonehara, K., and Roska, B. (2013). Ambient illumination toggles a neuronal circuit switch in the retina and visual perception at cone threshold. Neuron *78*, 325–338.

Franke, F., Quian Quiroga, R., Hierlemann, A., and Obermayer, K. (2015). Bayes optimal template matching for spike sorting - combining fisher discriminant analysis with optimal filtering. J. Comput. Neurosci.

Fiscella, M., Farrow, K., Jones, I.L., Jäckel, D., Müller, J., Frey, U., Bakkum, D.J., Hantz, P., Roska, B., and Hierlemann, A. (2012). Recording from defined populations of retinal ganglion cells using a high-density CMOS-integrated microelectrode array with real-time switchable electrode selection. J. Neurosci. Methods *211*, 103–113.

Frey, U., Egert, U., Heer, F., Hafizovic, S., and Hierlemann, A. (2009). Microelectronic system for high-resolution mapping of extracellular electric fields applied to brain slices. Biosens. Bioelectron. *24*, 2191–2198.

Frey, U., Sedivy, J., Heer, F., Pedron, R., Ballini, M., Mueller, J., Bakkum, D., Hafizovic, S., Faraci, F.D., Greve, F., et al. (2010). Switch-Matrix-Based High-Density Microelectrode Array in CMOS Technology. IEEE J. Solid-State Circuits *45*, 467–482.

Ghanem, A., Kern, A., and Conzelmann, K.-K. (2012). Significantly improved rescue of rabies virus from cDNA plasmids. Eur. J. Cell Biol. *91*, 10–16.

Marre, O., Amodei, D., Deshmukh, N., Sadeghi, K., Soo, F., Holy, T.E., and Berry, M.J. (2012). Mapping a complete neural population in the retina. J. Neurosci. Off. J. Soc. Neurosci. *32*, 14859–14873.

Müller, J., Ballini, M., Livi, P., Chen, Y., Radivojevic, M., Shadmani, A., Viswam, V., Jones, I.L., Fiscella, M., Diggelmann, R., et al. (2015). High-resolution CMOS MEA platform to study neurons at subcellular, cellular, and network levels. Lab Chip *15*, 2767–2780.

Oyster, C.W. (2006). The human eye: structure and function (Sunderland, Mass.; Basingstoke: Sinauer Associates ; Macmillan [distributor]).

Prentice, J.S., Homann, J., Simmons, K.D., Tkačik, G., Balasubramanian, V., and Nelson, P.C. (2011). Fast, scalable, Bayesian spike identification for multi-electrode arrays. PloS One *6*, e19884.

Remtulla, S., and Hallett, P.E. (1985). A schematic eye for the mouse, and comparisons with the rat. Vision Res. *25*, 21–31.

Roska, B., and Werblin, F. (2001). Vertical interactions across ten parallel, stacked representations in the mammalian retina. Nature *410*, 583–587.

Taylor, W.R., and Vaney, D.I. (2002). Diverse synaptic mechanisms generate direction selectivity in the rabbit retina. J. Neurosci. Off. J. Soc. Neurosci. *22*, 7712–7720.

Wickersham, I.R., Finke, S., Conzelmann, K.-K., and Callaway, E.M. (2007a). Retrograde neuronal tracing with a deletion-mutant rabies virus. Nat. Methods *4*, 47–49.

Wickersham, I.R., Lyon, D.C., Barnard, R.J.O., Mori, T., Finke, S., Conzelmann, K.-K., Young, J.A.T., and Callaway, E.M. (2007b). Monosynaptic restriction of transsynaptic tracing from single, genetically targeted neurons. Neuron *53*, 639–647.